Key controls on hydrocarbon retention and leakage from structural traps in the Hammerfest Basin, SW Barents Sea: implications for prospect analysis and risk assessment

Isabel Edmundson[1], Atle Rotevatn[1], Roy Davies[2], Graham Yielding[3] and Kjetil Broberg[2]

[1] Department of Earth Science, University of Bergen, Allégaten 41, 5007 Bergen, Norway

[2] DEA Norge AS, Jåttåflaten 27, 4020 Stavanger, Norway

[3] Badley Geoscience Ltd, North Beck House, North Beck Lane, Spilsby PE23 5NB, UK

Abstract

Evidence of hydrocarbon leakage has been well documented across the SW Barents Sea and is commonly associated with exhumation in the Cenozoic. However, further study is required to understand what specific mechanism(s) facilitate such leakage, and why this occurs in some locations and not others. We use seismic and well data to quantify fault- and top-seal strength based on mechanical and capillary threshold pressure properties of fault and cap-rocks. Magnitude and timing of fault slip are measured to acknowledge the role that faults play in controlling fluid flow. Results strongly indicate that across-fault and top-seal breach by capillary threshold pressure, and top-seal breach by mechanical failure are highly unlikely to have caused hydrocarbon leakage. Instead, top-seal breach caused by both tectonic reactivation of faults and fault dilation associated with de-glaciation processes is likely to have facilitated widespread hydrocarbon leakage from structural traps. The results presented herein have implications for understanding mechanisms and locations of hydrocarbon leakage from structural traps across basins worldwide. This is particularly important for exploration and production of hydrocarbons since seal failure is the main cause of dry wells.

Introduction

Accumulation and retention of hydrocarbons within a structural trap depends upon access to charge and the presence of a lateral-seal and top-seal (Fig. 1) (Dolson 2016). Given these are in place, it is the interplay between retention and charge that determines the height of the hydrocarbon column (Zieglar 1992). The charge is controlled by access to a mature source rock and the migration of hydrocarbons into a trap, whereas retention is controlled by the integrity of the cap rocks and faults that seal the trap.

Hydrocarbons may leak out of a trap across a fault (fault-seal breach) or through the cap rock (top-seal breach). Breach of the top-seal can occur by three different mechanisms: capillary breach, tectonic breach and mechanical failure (Corcoran & Doré 2002). For capillary breaching, the capillary threshold pressure of the cap rock must be overcome by the underlying buoyancy pressure of the hydrocarbon column (Downey 1994; Bretan et al. 2003). Tectonic breaching occurs when fault slip events cause the fault to extend through the cap rock forming a potential conduit that bypasses the top-seal (Cartwright et al. 2007). Mechanical failure is when the pore pressure in the reservoir exceeds the minimum horizontal stress and the tensile strength of the cap rock, creating mode I fractures in the cap-rock (Bjørkum et al. 1998; Ingram et al. 1999). Few studies have comprehensively assessed all of these mechanisms together, and none to our knowledge have done so over the Snøhvit field in the Hammerfest Basin using quantitative methods. Studies over the same basin have tended to focus on single processes to explain hydrocarbon leakage, such as mechanical seal failure (Makurat et al. 1992, Gabrielsen et al. 1997), fault reactivation (Hermanrud et al 2014; Mohammedyasin et al. 2016), differential uplift and tilting (Doré & Jensen 1996) and isostatic adjustment in response to ice retreat (Ostanin et al. 2013).

When assessing structural traps, fault-seal capacity must also be included to assess what hydrocarbon column height can be supported by a bounding or set of bounding faults (Færseth et al. 2007). Since faults tend to be lithologically and structurally heterogeneous along strike and dip, they may alternate between sealing and leaking behaviours, spatially but also temporally (Caine & Evans 1996; Yielding et al. 1997; Moretti 1998). Factors such as host and fault rock lithology and permeability, juxtaposition relationships, fault and fracture network permeability and connectivity, fluid pressure and type, and stress field orientation all affect a fault's transmissibility (Childs et al. 1997; Færseth et al. 2007; Ostanin et al. 2012; Fossen 2016). Therefore, predicting fault-controlled fluid flow is a complex exercise, and a significant amount of work has been dedicated to modelling the sealing capacity of faults and fault systems based on capillary threshold pressure properties (Yielding et al. 1997; Sperrevik et al. 2002; Bretan et al. 2003, 2017). Equally, the hydraulic properties of individual faults and their control on fluid flow are well known and have been discussed at length (e.g. Knipe 1993; Barton et al. 1995; Moretti 1998; Fredman et al. 2007; Faulkner et al, 2010; Wibberley et al. 2017). Since fault behaviour and its effect on fluid flow is inherently dynamic rather than static, analysis of how fault activity changes over time must also be considered.

In order to comprehensively assess the role of fault-seal and top-seal breach in causing hydrocarbon leakage, we investigate seal and retention processes in an area where there is good control on present hydrocarbon column heights as well as paleo-hydrocarbon column heights, namely the Snøhvit gas field in Hammerfest Basin. Here, the recurring presence of deep paleo-oil shows, seismic imaging of gas chimneys, seabed pockmarks and the high number of discoveries confirm that hydrocarbon charge is abundant (Doré & Jensen 1996; Chand et al. 2012; Ostanin et al. 2012, 2013; Duran et al. 2013). Nevertheless, most traps in this area are underfilled due to partial leakage; this makes the Hammerfest Basin an excellent area to study the key controls on seal integrity and breaching.

The paleo-columns show that all traps in the study area have undergone partial leakage, and through this study, we aim to investigate the mechanisms by which leakage occurred. The main aim is addressed through the following objectives: i) to quantify the sealing capacity of the cap rock and bounding faults to assess whether top-seal breach or lateral-seal breach is most likely to have facilitated hydrocarbon leakage across the Snøhvit gas field; ii) to evaluate the mechanism(s) by which leakage occurred: mechanical failure, capillary breaching or tectonic breaching; and iii) identify the locations at which fluid leakage is most likely to occur.

To do this, actual in-place hydrocarbon column heights measured across the Snøhvit field were compared with a number of theoretical maximum hydrocarbon column heights based on fault and top-seal properties. Furthermore, analysis of vertical displacement distributions were used to investigate the role of fault activity and reactivation in causing fluid leakage.

The results of this paper offer new insights into key mechanisms for seal integrity and breaching in hydrocarbon traps, which can be applied in hydrocarbon exploration. The results are equally applicable to assess seal risk factors associated with subsurface storage of CO2, hydrogen and natural gas.

Geological evolution of the SW Barents Sea

The SW Barents Sea has a prolonged, multi-phase tectonic history, which following the Caledonian Orogeny in Siluro-Devonian times has been dominated by protracted rifting from

Upper Paleozoic through to Cenozoic times. Throughout this period, a series of rift basins developed (Fig. 2) along two major established structural grains inherited from the Caledonian and Uralian (Carboniferous-Triassic) orogenies (Doré & Jensen 1996; Gudlaugsson et al. 1998; Faleide et al. 2008; Henriksen et al. 2011). Three major stages of rifting dominate; late Devonian to early Carboniferous (?), Middle Jurassic to Early Cretaceous and Early Cenozoic, each consisting of several tectonic phases (Faleide et al. 1993). Rifting during the Middle-Late Jurassic to Early Cretaceous established basin highs and lows including the Hammerfest Basin, Loppa High, and Finnmark Platform (Gabrielsen 1984; Faleide et al. 1993). As the focus of rifting, subsidence and accommodating strike slip movements shifted westwards, these basins remained relatively stable and experienced little subsidence from the early Cretaceous onwards (Gabrielsen & Kløvjan 1997). Meanwhile continuation of local faulting, subsidence and sedimentation established the Tromsø and Bjørnøya basins to the west (Faleide et al. 1993; Henriksen at el. 2011). These basins are filled with thick Cretaceous post-rift deposits, which largely covered the previously established high and lows (Faleide et al. 1993). In response to repeated rifting and weakening of the continental crust through Mesozoic-Ceonzoic times, a regional shear zone formed along the western margin. This initiated the opening of the Norwegian Greenland Sea in the Eocene, which was accompanied by regional magmatism and sea-floor spreading. Development of the passive margin continued as the Norwegian - Greenland Sea deepened in response to sediment loading (Faleide et al. 2008).

The cause and onset of subsequent compressional deformation and associated uplift is debated but thought to have initiated in Miocene times due to plume-enhanced ridge push (Faleide et al 1993; Doré and Lundin 1996; Lundin & Doré 2002; Cavanagh et al. 2006). Ongoing continental shelf glaciations in the Pliocene-Pleistocene covered the entire Barents Sea.

Compensating isostatic uplift and glacio-eustatic lowering of the sea-level is thought to have contributed to further uplift and erosion with total erosion rates estimated at between 500m and 1500m (Nyland et al. 1992; Faleide et al. 1993; Cavanagh et al. 2006; Chand et al. 2012; Duuran et al. 2013; Ostanin et al. 2017).

Structure of the Hammerfest Basin and elements of the petroleum system

The Hammerfest Basin itself is an ENE/WSW trending basin that is structurally bounded by the Loppa High to the North, the Finnmark Platform to the south, the Bjarmeland Platform to the east and the Ringvassøy-Loppa Fault Complex to the west (Fig. 2). The basin is 150km long and 70km wide, and is largely characterized by two major fault trends, E-W and NNE-SSW. Activation of both high-angle normal faults and listric faults during Middle-Late Jurassic to Early Cretaceous rifting established classic rotated fault blocks and horst structures, which have been the main targets for early exploration (Gabrielsen et al 1990; Faleide 2008; Hermanrud et al. 2014).

Results from exploration across the Hammerfest Basin have identified a number of source and reservoir units of Triassic to Cretaceous age (Duran et al. 2013) (Fig. 3). The most prolific reservoir unit in the Hammerfest Basin is the high quality shoreface/shallow-marine deposits of the Early to Middle Jurassic Stø Formation (Doré 1995; Henriksen et al. 2011; Hermanrud et al. 2014). Additional reservoirs have also been proven in sandstones of Triassic and Cretaceous age (Johansen et al. 1993; Larsen et al 1993). Overlying the Stø Formation is the Upper Jurassic Hekkingen Formation, an organic-rich shale rock deposited during anoxic marine conditions, which forms a cap rock. The Snøhvit field is thought to be charged by the Hekkingen Formation in addition to the Triassic Snadd and Kobbe Formations (Duran et al. 2013).

Exploration results from the SW Barents Sea have been largely disappointing (Doré & Jensen 1996). Despite a high technical success rate of exploration drilling (over 50% have discovered hydrocarbons in the last five years), there are only two producing fields, Snøhvit and Goliat. Negative effects of the Cenozoic uplift event have been largely blamed for disrupting the petroleum system. Issues such as reactivation of faults, erosion of top seal, gas expansion, differential tilting, secondary migration and cooling of source rocks have all been proposed as causing depleted targeted reservoirs (Doré 1995; Doré & Jensen 1996; Doré & Lundin 1996; Duran et al. 2013; Hermanrud et al. 2014; Ostanin et al. 2017).

Mechanisms by which hydrocarbons can leak from structural traps

Across the Barents Sea, trap failure is the most common cause of dry wells, accounting for 41% of all failures (NPD 2018). For this reason, it is important to thoroughly assess the variety of mechanisms by which seal-breach can occur. They are: capillary threshold pressure leakage, mechanical failure, tectonic breaching and molecular transport (Corcoran & Doré 2002). The first three methods are discussed in more detail below. Molecular transport, otherwise known as diffusion can also cause hydrocarbon leakage but the process requires tens of millions of years to significantly affect the level of hydrocarbon volumes and so is thought to contribute only a very minor role to reducing hydrocarbon columns (Schlömer & Krooss 1997). It is therefore not considered in this study.

Capillary threshold pressure is a force that the non-wetting fluid (typically hydrocarbon in this example) must overcome in order to replace the wetting fluid (typically water) and is calculated as follows:

$$P_C = (2ɣ \times \cos \theta)/r \qquad \text{(Equation 1)}$$

P_C = capillary threshold pressure

r = pore throat radius

ɣ = interfacial tension

θ = wettability

In a stable water-wet system, the interfacial tension and wettability remain relatively constant (Dolson 2016). It is therefore the pore throat radius that exerts the biggest influence on the capillary threshold pressure and will usually change according to lithology, burial and diagenesis. For example, fine-grained lithologies, such as phyllosilicates have small pore throat radii, which increases the capillary threshold pressure (Yielding 2002). Lithologies that exhibit very small pore throats, such as evaporites and shales are therefore effective seals (Grunau 1987; Downey 1994; Ingram et al. 1999; Corcoran & Doré 2002; Dolson 2016). The competing force against the capillary threshold pressure is the buoyancy exerted by the underlying hydrocarbon leg. The buoyancy is calculated as follows:

$$\Delta P = (\rho_w - \rho_h) \times g \times h \qquad \text{(Equation 2)}$$

ΔP = buoyancy

ρ_w = water density

ρ_h = hydrocarbon density

g = gravitational potential

h = height of the hydrocarbon column (m)

When the buoyancy exceeds the weakest part of the capillary seal, equivalent to where the largest pore throat is found, leakage occurs (Dolson 2016). Because of capillary hysteresis, leakage continues until the buoyancy pressure is only a half to a third of the threshold pressure (Vassenden et al. 2014), and then leakage ceases. Further leakage can then occur if the buoyancy is boosted either because of an increase in the hydrocarbon column due to additional charge or a decrease in the hydrocarbon density.

The second mechanism by which leakage can occur across the top-seal is by mechanical failure and usually occurs in an environment of high fluid pressure (Aydin 2000). Type mode I fractures form when the buoyancy force of the hydrocarbon column exceeds the minimum in-situ horizontal stress and tensile strength of the rock (Ingram et al. 1999). The resulting formation of hydraulically driven fractures will rapidly increase the permeability of the cap rock, providing conduits through which fluids may escape through an otherwise impermeable sealing unit (Ostanin et al. 2012).

The third mechanism causing top seal breach is tectonic breaching, i.e. loss of seal integrity by faulting or fault reactivation. During movement, faults can dilate, particularly those trending parallel or sub-parallel to the maximum horizontal stress, which increases permeability and facilitates fluid flow (Doré & Jensen 1996; Doré & Lundin 1996). In the Barents Sea, fault reactivation in the Cenozoic (Faleide et al 1993; Doré & Lundin 1996; Lundin & Doré 2002; Cavanagh et al. 2006) post-dates the charge event (Ostanin et al. 2017) and is a potential factor that may have contributed to causing leakage from structural traps (Knipe 1993; Doré & Jensen 1996; Moretti 1998; Aydin 2000; Corcoran & Doré 2002; Cavanagh et al. 2006; Hermanrud et al. 2014); this will be discussed further later in the paper.

Dataset

This study uses subsurface data that covers the six major hydrocarbon filled traps that make up the Snøhvit gas field. They are; Snøhvit Nord, Snøhvit central, Askeladd (north and south) and Albatross (north and south). The dataset consists of two overlapping public 3D seismic reflection cubes (surveys ST0306 and ST8320, location shown in Figure 2) that have a combined aerial coverage of approximately 1270 km^2, plus 13 exploration wells with wireline log data. The migrated post-stack seismic data is of good to very good quality, allowing a high confidence in detailed structural interpretation. Further de-noising and color inversion over the Middle – Jurassic intervals of both seismic datasets helped improve interpretations, especially at horizon-fault and fault-fault intersections. Composite logs and available well reports were used to correlate stratigraphic markers to seismic reflectors, identify hydrocarbon-water contacts and corroborate lithology types. The seismic data and interpretation products were converted to depth using a regional velocity cube.

Method

In order to investigate mechanisms responsible for top- and/or fault-breach, methods in this study have been chosen to quantify top-seal and fault-seal capacity, and assess fault reactivation history. Calculation of in-place and paleo-column heights is used to examine the extent of leakage from the six structural traps within the Snøhvit gas field. Modelling and calculations (described in the following subsections) are used to assess across- and top-seal strength, and the corresponding computed maximum hydrocarbon column height that could be supported. The theoretical and actual in-place column heights are compared to assess if leakage is controlled by a particular mechanism that causes top- or fault-seal breach. Finally, T-z plots are constructed to constrain the timing of fault slip and mechanism of reactivation.

Column height measurement and terminology

The heights of discovered hydrocarbon columns in a number of structures across the Snøhvit gas field were calculated. Depths necessary to calculate such column heights and associated trap dimensions along with related terminology are shown in Figure 1. Formation test results, resistivity measurements and well completion reports were used to identify fluid contacts depths. Interpretation of the top reservoir (Stø Formation) on 3D seismic data, followed by depth conversion, was used to calculate the reservoir depth at the well location, the apex of the trap and the spill point. To assess the likelihood of any paleo-contacts, the depth of the deepest paleo oil-show was also noted from well and core reports.

Seismic interpretation and establishment of a 3D structural model

Eleven horizons and over 150 faults were picked across the dataset and refined using the variance attribute computed across both seismic cubes. The variance attribute highlights abrupt changes in seismic amplitude and is therefore a useful tool to detect breaks in seismic reflectivity, such as a fault. The TrapTester software was used to construct a structural model consisting of a number of fault-fault intersections (branch lines) and footwall/hangingwall – fault intersections using depth converted fault and surface interpretations (Allan 1989; Knipe 1997; Knipe et al. 1997; Bretan 2017).

Petrophysical assessment: Volume of clay (V_{clay}) and porosity calculation

The V_{clay} curve is a key parameter that is required to calculate the shale gouge ratio (SGR) algorithm, an input which is necessary to estimate the capillary threshold pressure of the fault, which in turn is an indicator of the fault's seal strength. The gamma ray, neutron and density logs were used to quantitatively derive the volume of shale (V_{shale}) encountered by the borehole using methods detailed in Rider & Kennedy (2011). Typically, shale comprises of 60% clay, and so the V_{shale} log was reduced by 40% to account for non-clay minerals, resulting in the final V_{clay} log (Bhuyan & Passey 1994). The V_{clay} log was calculated for each of the 10 successful discovery wells across the Snøhvit field and cross-checked against well log and composite reports.

Similar to lateral seal, the estimation of the top seal's strength also relies on calculation of some particular petrophyscial properties. The porosity is used as a proxy to estimate what seal type the cap rock is, from which the capillary threshold pressure is estimated (Cavanagh & Wildgust 2011). The porosity is calculated using the density log measured across the Hekkingen Formation using methods detailed in Rider and Kennedy (2011). Porosity results for each well were firstly averaged across the Hekkingen formation to give one porosity reading per well. These well values were then averaged to give four values, one for each of the Albatross, Askeladd, Snøhvit central and Snøhvit Nord structures.

Calculation of the theoretical maximum hydrocarbon column height based on the capillary threshold pressure

The Trap Analysis module within the TrapTester software was used to estimate the maximum hydrocarbon column that could be supported by the capillary threshold pressure of the bounding faults (Bretan 2017). The maximum column height occurs when the buoyancy pressure of the hydrocarbon column is equal to the capillary threshold pressure of the fault(s):

$$h_{max} = P_c/(g\times(\rho_{w} - \rho_h) \quad \text{(Equation 3)}$$

h_{max} = maximum hydrocarbon column height

ρ_w = water density

ρ_h = hydrocarbon density

g = gravitational potential

P_c = capillary threshold pressure

The capillary threshold pressure of the fault cannot be measured directly so is estimated using the SGR algorithm. The SGR is an estimate of the proportion of fine-grained material entrained into the fault gouge, which takes into account the distribution of clay (represented by the V_{clay} curve) and displacement across the fault (Yielding et al. 1997). The SGR can then be empirically calibrated to a corresponding capillary threshold pressure using a global dataset that compares across-fault pressure difference or buoyancy pressure with the fault's SGR. Work by Yielding (2002) and Yielding et al. (2010) provides a thorough explanation of how this calibration technique has been compiled and utilized to estimate the maximum fault seal strength and therefore, the maximum hydrocarbon column height that can be supported by the fault. Note that the Albatross north structure was excluded from analysis because of its large gas chimney, which partially obscures the seismic data to the east. Without good quality input data, the model would not reliable and any results would be highly speculative and unreliable. The input data used to model the maximum hydrocarbon column that can be supported by the faults is shown for each structure in table 1.

Even with good quality data, challenges continue to face fault seal analysis methods and are typically a result of the uncertainties associated with inputs and calibration techniques (Dewhurst & Yielding 2017). For this reason, a range of fault seal strengths and associated column heights were derived by varying two major inputs used by the model, both of which carry a degree of uncertainty: the V_{clay} curve and uplift correction. The uplift correction refers to the difference (if any) between the current and maximum burial depth of the reservoir. The V_{clay} was varied by plus/minus 10% to account for uncertainty in the parameters chosen when estimating the phyllosilicate content from the gamma-ray, and combined neutron and density logs. The base rate uplift (refer to table 1) was decreased by 250m and increased by 250m and 500m to account for uncertainty in erosion estimates. The maximum burial of the fault determines if the effect of quartz cementation should be included, which in practice is implemented by means of the different seal failure envelopes used to calibrate the SGR to a capillary threshold pressure (Yielding et al. 2010). This effect can significantly change the seal strength of the fault.

Calculation of the theoretical maximum column based on the mechanical and capillary strength of the top seal

This method assumes that the maximum column height is controlled either by the mechanical strength or the capillary strength of the cap rock. The maximum column based on the mechanical top seal strength is calculated as follows:

$$h_{max} = o \times [(f\nabla - w\nabla)/(w\nabla - h\nabla)] \qquad \text{(Equation 4)}$$

h_{max} = maximum hydrocarbon column height

o = overburden in metres

$f\nabla$ = fracture gradient

$h\nabla$ = hydrocarbon gradient

$w\nabla$ = water gradient

The fracture gradient, hydrocarbon gradient and water gradient are routinely measured in the wells from leak off and repeat formation tests, and are typically found in well reports (Dolson 2016).

The capillary threshold strength of the top seal rock is estimated based on its facies type, which is determined by its porosity. Calculated porosity values from petrophyscial evaluation are plotted on a porosity/depth plot that contains five predefined curves, each representing a different facies type (Peolchau et al. 1997). The cap rock facies type is indicated by the curve that best matches the plotted porosity/depth measurements. Given the facies type of the cap rock is now known, the capillary threshold pressure can be estimated using results from laboratory tests, which use a mercury/air system on core samples to mimic the hydrocarbon/water system in the subsurface (Ibrahim et al. 1970; Schloemer & Kross 1997; Sperrevik et al. 2002). Five depth-threshold pressure curves are calculated for each different facies type (Cavanagh & Wildgust 2011). Therefore, by using a combination of petrophysics and calibration techniques, the capillary threshold pressure of the cap rock and the maximum hydrocarbon column height that it can support can be estimated using the two equations 5 and 6 below (Dolson 2016).

$$P_{c\,(hw)} = \{(\gamma_{hw} \times \cos\theta_{hw})/(\gamma_{mecury/air} \times \cos\theta_{mercury/air})\} \times Pc_{air/mercury} \qquad \text{(Equation 5)}$$

$$h_{max}\,(\mathrm{ft}) = P_{c\,(hw)}/(0.433 \times (\rho_w - \rho_h)\} \qquad \text{(Equation 6)}$$

$P_{c\,(hw)}$ = capillary threshold pressure (hydrocarbon/water system)

$P_{c\,(air/mercury)}$ = capillary threshold pressure (air/mercury system)

γ_{hw} = interfacial tension (hydrocarbon/water system)

$\gamma_{mecury/air}$ = interfacial tension (mercury/air system)

θ_{hw} = contact angle (hydrocarbon/water system)

$\theta_{mercury/air}$ = contact angle (mercury/air system

Quantifying the slip and timing of fault reactivation

Throw-depth (T-z) plots were constructed for all bounding faults that define the six structural traps in the Snøhvit gas field. T-z plots give insights into fault nucleation and propagation, allowing periods of syn-sedimentary fault to be differentiated from periods of post-sedimentary faulting (Baudon & Cartwright 2008; Tvedt 2013). In this case, they are particularly relevant for indicating any fault movement that post-dates the onset of charge from the Hekkingen Fm. in the Late-Cretaceous (Ostanin et al. 2013). Profiles were constructed by placing the list of measured horizons in chronological order on the y-axis against the corresponding throw on the x-axis. This process was repeated along each fault over a defined interval, which is determined by the fault length. Throw-depth plots were constructed every 50 metres for faults up to 3500 metres long, 150m for faults between 3500 and 8000 metres, 200 metres for faults between 8000 and 15000 metres, and 250 metres for faults exceeding 15000 metres.

Results

Measured in-place column heights

All wells used in this study recorded gas in the Upper Jurassic Stø reservoir unit, whilst the Snøhvit central structure also contains an 11-17 metre oil leg in the same formation as shown in Figure 4. Measured column heights in the 10 discovery wells are all shorter than their corresponding trap heights; these traps are therefore all referred to as underfilled. However, the degree of underfilling across the field is variable. For example, well 7120/8-1 (Askeladd north) has a hydrocarbon column height of 155m, equivalent to 67% of the trap height. Well 7121/7-2 (Albatross south), on the other hand, discovered a 36m column of hydrocarbons, equivalent to 37% of the trap height. These two wells represent the most filled and least fill structures, respectively. The average proportion of hydrocarbon fill in the 10 discovery wells is 53%. In addition, all discoveries contained paleo-oil shows located deeper than the hydrocarbon-water fluid contact and in some cases down to the spill-point.

Computed maximum column heights held by fault seal

A set of maximum hydrocarbon column heights that could be held by laterally bounding faults were computed based on the capillary strength of the fault seal, using the TrapTester software. Results show that all bounding faults have capillary threshold pressures that are able to support a column of gas that is between 86-158% taller than the actual measured in-place column. Additionally, in three out of five cases, fault seal is strong enough to support a hydrocarbon column that is taller than the trap height. Individual results and comparisons between the calculated maximum column heights, the actual column height and trap height for each structure is discussed below and visualized in Figures 5 and 6.

For the Snøhvit Nord, Snøhvit central and Askeladd north structures, the model predicts that the bounding faults have sufficient seal capacity to support a hydrocarbon column that exceeds both the actual column height and the height of the structure. Unlike the other structures, the model predicts the faults delineating Albatross south and Askeladd south do not have sufficient seal capacity to support a hydrocarbon column that is equivalent to or larger than the trap height. In all cases, the faults are still able to support a taller column than what was discovered in-place. This result remained the same when the uplift correction and V_{clay} input were varied during sensitivity testing.

Calculated maximum column heights based on the top seal capillary threshold pressure

Estimated total porosities of the Hekkingen cap rock range from 0.11% to 0.15% at depths of between 1813m and 2338m. The four porosity values of the Hekkingen formation measured for the Snøhvit Nord, Snøhvit central, Askeladd and Albatross structures fall consistently on the porosity-depth curves that represent tight or low porosity seals (Fig. 7a). Based on this information, the threshold pressure – depth curves (Fig 7b) are used to calculate two capillary threshold pressures of the Hekkingen formation, one for a tight shale and one for a low porosity shale. The resulting range of hydrocarbon column heights that can be supported by these two capillary threshold pressures curves are plotted against depth, shown in Figure 8 (red curves). Unsurprisingly, the tight seal curve is able to support a taller column of hydrocarbons than a low porosity shale seal at any given depth. Computed maximum column heights, based on low porosity shale properties offer the best approximation to actual hydrocarbon column heights. However, it is evident that the computed maximum hydrocarbon column heights consistently exceed actual hydrocarbon column heights measured across the Hammerfest Basin.

Calculated maximum column heights based on top seal mechanical properties

This calculated maximum hydrocarbon column calculated using equation 4 was plotted against overburden thickness (Fig. 8, green and brown curves). As the overburden thickness increases, the maximum height that can be supported by the mechanical strength of the rock increases linearly. At an overburden thickness of 500 metres, the Hekkingen top seal can mechanically support an oil column of almost 500m or a gas column of 300m. Hydrocarbon column heights estimated in this way consistently and significantly exceed the discovered in-place column heights measured across the Hammerfest Basin.

Fault reactivation

All bounding faults for each structure have been grouped into three categories according to shared T-z profile geometries (Fig. 9). Based on these profiles presented herein, we can make interpretations concerning the nature of fault slip and evidence for fault reactivation (Tvedt et al. 2013). Typical to all plots is a maximum throw recorded in the early to Middle Jurassic strata after which the throw consistently decreases across Middle Jurassic to Early Cretaceous strata. The point of maximum throw suggests fault nucleation occurred within middle Jurassic strata or deeper. Further differences in recorded throw across Early/Middle Cretaceous to Paleogene strata define each of the three fault categories.

A summary of these three different styles of fault evolution is discussed below and summarized in Figure 10. Category 1 faults have a throw profile which contains two throw maxima separated by a throw minimum. This is characteristic of a fault that after being buried has experienced renewed fault growth/reactivation, but where fault reactivation at depth has led to the nucleation of a new fault in the overburden, which has subsequently propagated down to vertically link with the parent fault (Cartwright et al. 1995; Baudon and Cartwright 2008b; Jackson & Rotevatn 2013; Rotevatn & Jackson 2014). The point of linkage is represented by the displacement minimum on the T-z plot (Tvedt 2013). Category 2 faults have also been reactivated after initial growth and burial. However, a more gradual upward decrease in throw across Early to Middle Cretaceous strata suggests fault reactivation was achieved by upward propagation of the existing fault into the overburden, referred to as blind upward fault propagation (Baudon & Cartwight 2008c; Jackson & Rotevatn 2013; Tvedt et al. 2013; Fossen 2016). Category 3 faults do not register any subsequent throw in sediments older than Early Cretaceous, and therefore are interpreted as not having been reactivated.

It should be noted that not all profiles measured for the same fault are identical in shape and there may be some indication of a fault exhibiting a dual behaviour in its reactivation style. Such variation in throw distribution along strike illustrates the complexity and heterogeneity of fault growth. It is the overall geometry of the throw distribution shown by the T-z plots, which determines the fault's category.

Discussion

Across-fault breach

Fault seal analysis and a series of sensitivity tests reveal that the bounding faults for each structure are able to seal significantly taller columns of hydrocarbon than those discovered. Fault-seal work carried out by Bernal (2009) on faults defining the Askeladd field contains similar findings. The SGR calculated for all modelled bounding faults equates to a high capillary threshold pressure meaning across-fault breach will only occur when a very large buoyancy force exceeds this capillary threshold pressure (Bretan et al. 2003). To achieve such a buoyancy force, the column of hydrocarbons pushing against the fault would have to be over twice as high than the actual column height in all cases, bar one. In three out of the five assessed structures, the maximum calculated column height also exceeds the paleo-hydrocarbon column, the height between the apex and the deepest oil show. Therefore, it is highly unlikely that the buoyancy force exerted by the hydrocarbon column height has exceeded the capillary threshold pressure of the bounding faults, which rules out the influence of across-fault breach as a leakage mechanism.

Top-seal breach based on the cap rock properties

Well tests indicated that the Snøhvit field is hydrostatically pressured. Therefore, in order to induce sufficient overpressure to fracture the cap-rock, the buoyancy force would have to be significantly higher. Calculations show that such the hydrocarbon column would have to be several hundred metres higher than the actual column height to achieve such a force (Fig. 8). This strongly suggests that top-seal breach by mechanical failure is not a likely control on the discovered column heights. Furthermore, despite the thickness of the top seal varying between 26m and 111m across the Snøhvit field, a study across the entire Hammerfest Basin concluded that cap rock thickness in this area also has no correlation with column heights observed in wells (Henriksen et al. 2011). It is would therefore be unwise to use the mechanical strength of the cap rock as the sole method to estimate column heights in yet-to-find prospect or appraisal scenarios since it would lead to significant overestimations. Work by Watts (1987) and Grunau (1987) on cap rock properties suggest that this is relevant not only for the Hammerfest Basin but also for other global basins that are hydrostatically pressured.

The computed maximum hydrocarbon column heights, based on the capillary strength of a low porosity shale seal, offers a closer approximation to actual column heights. Nevertheless, theoretical hydrocarbon column heights estimated in this way consistently exceed what is observed. Calculations indicate that the capillary threshold force of the cap rock is high and capable of sealing a much taller column of hydrocarbons than in-place. This implies that the buoyancy force exerted by the actual hydrocarbon column height is not enough to overcome the capillary threshold pressure of the cap rock (Grunau 1987; Bretan et al. 2003). For this reason, it is unlikely that present-day hydrocarbon column heights across the Hammerfest Basin are limited by capillary leakage through the top seal.

Top seal-breach by faulting

Using observations from interpreted seismic data, Hermanrud et al. (2014) discussed the importance of column restricting faults in controlling column heights measured in the Hammerfest Basin. According to Hermanrud et al. (2014), column-restricting faults are faults that support no hydrocarbon column, meaning the fluid contact and top reservoir surface intersect at depth when they meet the fault. Such faults may suggest that vertical leakage along the fault has occurred, which controls the maximum column height. However, not all faults and all parts of the same faults exert this uniform control on fluid flow. Vertical leakage may occur along *some* faults but certainly not all since the current accumulations that constitute the Snøhvit gas field are all retained within structural traps. This is not unexpected given that faults are heterogeneous by nature and their sealing properties will vary in time and space (Caine et al. 1996; Childs et al. 1997; Moretti 1998; Farsæth et al. 2007; Fredman et al. 2007; Rotevatn et al. 2013; Wibberley et al. 2017).

A factor that may affect the sealing properties of faults is fault reactivation. In this study, knowing the *timing* of fault reactivation is essential, since faults or parts of faults that were active at a time that post-dates the time of reservoir charge may facilitate vertical leakage and top-seal breach (Aydin 2000; Duran et al. 2013). Based on T-z profiles, all measured faults recorded significant throws across Jurassic to Early Cretaceous strata representing the main period of faulting that occurred between the Middle Jurassic to Early Cretaceous times (Gabrielsen 1984; Faleide et al. 1993; Henriksen et al. 2014). Category 1 and 2 faults experienced further slip after the main Middle Jurassic to early Cretaceous rifting event that established the present high and lows within the Hammerfest Basin (Gabrielsen 1984; Faleide et al. 1993). The shape of the throw distribution recorded by the T-z plots gives an indication of whether fault slip occurred during or after sedimentation. An asymmetric throw profile, shown by a rapid decrease in throw from the maximum, is typical of a fault that has an unrestricted lower tip-line but a restricted upper tip-line due to the presence of a free surface (Baudon & Cartwright 2008a; Jackson & Rotevatn 2013; Tvedt et al. 2013). This profile is characteristic of syn-sedimentary fault slip. Throw gradients that increase and decrease gradually to and from the throw maximum indicate that both the upper and lower-tip lines of the fault are unrestricted. This profile is characteristic of fault-slip that occurred post-sedimentation in unconfined conditions (Peacock & Sanderson 1991).

It is therefore proposed that reactivation of both category 1 and 2 faults occurred after the Late Cretaceous. Category 1 faults that have been reactivated by vertical dip linkage exhibit a gradual increase and decrease in throw forming a second throw maximum, suggesting that fault reactivation occurred after the deposition of Late Cretaceous sediments. Category 2 faults reactivated by blind-fault propagation record a very gradually decreasing throw across Early/Middle/Late Cretaceous and Palegoene strata indicating that fault reactivation was post-depositional and occurred after the Late Cretaceous/Early Paleogene times. This evidence indicates that the reactivation of category 1 and 2 faults post-dates the time that the Snadd, Kobbe and Hekkingen source rocks all entered the oil window (Ostanin et al. 2017). This relative timing between fault movement and charge is important and strongly indicates that hydrocarbons were in place before fault reactivation occurred.

The results from T-z plots therefore provide three important pieces of information. Firstly, that some but not all faults were reactivated after the major source rocks reached maturity and began to charge surrounding reservoirs. Secondly that the style of fault reactivation was not uniform across the Snøhvit field. Two different styles of fault reactivation were identified: i) upward propagating reactivation, and ii) nucleation of new faults in the overburden that subsequently linked vertically with their parent fault at depth. Thirdly, the distribution of category 1 and 2 faults could indicate likely locations of fault-controlled leakage (Fig. 11).

Gas leaking upwards along faults may accumulate in the overburden indicated in many cases by amplitude brightening and zones of dim or blank reflectivity (Ostanin et al 2012). Assessing the distribution and locations of shallow gas indicators, for example bright amplitude features, pockmark and mud diapers provides good evidence for faults acting as conduits for fluid flow and has been well documented across the southwestern Barents Sea (Cartwright et al. 2007; Chand et al. 2012; Ostanin et al. 2012; Simmenes et al. 2017). To test whether the reactivated (category 1 and 2) faults may have controlled leakage from hydrocarbon traps, we assess the nature locations of such shallow gas anomalies relative to faults. The root mean square amplitude attribute was used to screen for amplitude anomalies in the shallow subsurface over a broad window across the late Cretaceous Kveite formation. Figure 12 shows the distribution of these amplitudes across the entire field. The distribution of bright amplitudes tend to cluster around faults and some fault networks but they do not always strictly follow major fault trends. This could be due to lateral migration of fluids away from the fault, whilst numerous other factors associated with seismic acquisition and processing, such as lithological changes, which can produce similar seismic signatures (Kearey et al. 2013; Simm & Bacon 2014). However, there is direct evidence of amplitude brightening associated with two category 2 faults that define the Askeladd north and Snøhvit central structures, shown in Figure 12. This supports the notion that faults, which are known to have been reactivated (using interpretation of T-z plots) have facilitated hydrocarbon leakage from the reservoir to the shallower depths. Similar observations of gas chimneys, pock marks, fluid escape pipes and other fluid related anomalies by Ostanin et al (2013) and Mohammedyasin et al. (2016) offer further support that fault reactivation enabled vertical leakage of hydrocarbons along faults. This workflow shows that identifying likely locations of top-seal breach due to fault reactivation is perhaps best supported by combining measurements of fault slip activity with amplitude screening for shallow gas anomalies (Heggland 2005).

Fault reactivation can have significant consequences for fluid flow causing previous sealing faults to become conduits for fluid flow. It is well documented that fault reactivation can create new fractures and cause faults in brittle rock to dilate, which helps to rapidly and exponentially increase the number of permeable pathways through an impermeable seal (Doré and Lundin 1996; Ingram 1999; Wiprut & Zoback 2002). Such permeability enhancement may be particularly pronounced at and around fault intersections (Barton et al. 1995; Gartrell et al. 2004; Davatzes and Hickman 2005; Bastesen & Rotevatn 2012; Fossen & Rotevatn 2016, Dimmen et al. 2017). These zones are likely to contain a particularly high concentration of open fracture networks that act as channels helping to facilitate leakage of potentially large volumes of hydrocarbons (Gartrell et al. 2004; Tamagawa & Pollard, 2008; Hermanrud et al. 2014). An example of such an intersection is shown by an orthogonal pair of faults that trend N-S and E-W, which define the northwest corner of the Albatross (south) field. Both are category 2 faults, which may have contributed to significant drainage of this field, resulting in just 37% trap fill. Nevertheless, not all intersections between a pair of reactivated faults automatically indicates such a low trap fill. The pair of sub-orthogonal faults trending N-S and NE-SW, which define the Askeladd north structure have also been reactivated, yet the trap fill is 67%, the highest of all the structures that make up the Snøhvit field.

In addition to tectonically driven uplift, numerous studies have shown that glaciations in the Pliocene-Pleistocene have widely contributed to the major period of exhumation during the Cenozoic (Nyland et al. 1992; Cavanagh et al. 2006; Rodrigues et al. 2011). During this time, numerous pressure fluctuations in the basin are likely to have occurred in response to repeated glacial waxing and waning (Cavanagh et al. 2006). It is likely that conditions during this period of basin flux would have temporarily altered the stress-state of the deep regional faults (Fjeldskaar et al. 2000). In response, fault reactivation and/or accompanying fault dilation can occur, particularly along segments containing releasing-bends, which favor tensile failure (Zhang et al. 2008; Brandes et al. 2011). This significantly increase the fault rock's permeability and provides instant pathways that facilitate effective fluid flow from deep reservoirs to the shallower subsurface. Transportation of fluids through shallower Paleocene-early Eocene faults are thought to have caused a large number of paleo-pockmarks at the base Quaternary and on the seabed (Ostanin et al. 2013). This glacially induced fault leakage (Grollimund & Zoback 2003; Ostanin et al. 2017) may explain why underfilling is also recorded all structures in the Snøhvit field, not just those that are bounded by reactivated category 1 and 2 faults.

Based on the quantitative results of this study, it is highly unlikely that the mechanical and capillary strength of the top seal, or the capillary strength of the faults controlled hydrocarbon leakage. Given this result and above discussions, we propose that leakage was primarily controlled by temporarily conductive faults that were previously sealed to fluid flow. Measurements of fault slip and documentation of the effect of exhumation on fault behaviour (Nyland et al. 1992; Ohm 2008; Ostanin et al 2017) suggest that both fault reactivation and fault dilation caused the majority of faults to leak across the Snøhvit basin and this leakage may be particularly pronounced at fault intersections. Leakage that has occurred by these two means is primarily responsible for the measured hydrocarbon column heights that represent underfilling across the entire Snøhvit field. These findings are summarized schematically in Figure 13.

As demonstrated by this study, combining data that quantifies the growth history of structurally bounding faults with measurements of trap fill can be a powerful tool in assessing the role of fault-enabled hydrocarbon leakage. Further empirical measurements of fault and fault networks not included in this study, for example topology, would be an insightful addition to understanding how fault connectivity also affects fluid flow (Sanderson & Nixon 2015; Dimmen et al. 2017). Combining these approaches would contribute to improved assessments of seal integrity and associated estimations of the hydrocarbon column height during prospect assessment and pre-drill volume calculations. It seems appropriate to concentrate efforts on lowering the risk associated with seal analysis since trap failure is the most common cause of all wildcat dry wells, not only across the Barents Sea, but also globally (Knipe et al. 1997; Rudolph and Goulding 2017; NPD 2018).

Implications for prospect analysis

In resource assessments, the hydrocarbon column height distribution tends to have the highest impact on volume estimations. When assessing structural traps, a method that considers the role of fault reactivation, is likely to result in more realistic estimations of hydrocarbon column heights than an approach that disregards it. Introducing such an approach, as demonstrated in this study, can therefore help to reduce the overall uncertainty associated when calculating yet-to-find volumes (Demirem 2007). Equally, a more rigorous and empirical analysis of both the fault- and top-seal strength will help contribute to more reliable prospect risking. An improved understanding of if, how and where leakage has occurred can also help to reveal new play opportunities that have benefited from secondary migration (Farsæth et al. 2007). Such migration events in the Hammerfest Basin are thought to have redistributed hydrocarbons and in particular, oil to structurally shallow traps further to the east

(Johansen 1993; Doré et al. 2002; Ohm et al. 2008; Lerch et al. 2016). Workflows and lessons learnt in this study are relevant not only to the hydrocarbon industry but also to other projects concerned with understanding how cap rocks and faults effect fluid flow, for example in subsurface carbon sequestration or natural gas storage.

Conclusions

The key observations and conclusions from this work are:

- There is consistent underfilling of all the structures across the Snøhvit field. Poor retention rather than a lack of charge has limited the height of the in-situ hydrocarbon column heights. To elucidate how leakage has occurred, a series of computed maximum hydrocarbon column heights, based on a number of fault-seal and top-seal properties are compared to the observed in-place hydrocarbon columns. Integration of these results with measurements of fault-growth reveal how and where leakage has occurred.
- According to fault-seal analysis, across fault-breach by capillary threshold pressure is unlikely. The bounding faults defining each structure are capable of supporting a much taller hydrocarbon column compared to what has been discovered. For the majority of structures, the column height would have to be at least twice as tall for across-fault breach to occur.
- Calculations indicate that the Hekkingen cap rock is a tight to low-porosity shale. The capillary threshold pressure of this facies type is capable of supporting a column of hydrocarbons that far exceeds the actual column height recorded for each structure. Therefore, leakage of hydrocarbons across the top-seal by capillary threshold pressure is unlikely to have occurred.

- Leakage along conductive fractures caused by mechanical failure of the top-seal has very little influence on facilitating hydrocarbon leakage. Furthermore, predicting hydrocarbon column heights based on the mechanical strength of the top seal consistently results in significant overestimations and should be avoided.
- Tectonic-breaching is most likely to have caused hydrocarbon leakage. Fault reactivation and fault dilation associated with basin uplift in the Cenozoic, caused by active tectonics and de-glaciation, allowed hydrocarbons to leak along faults and breach the top-seal. This led to reduced hydrocarbon column heights, widespread basin underfilling and paleo-oil shows. Such fault-controlled leakage can be supported in some cases by locations of gas escape features shown as shallow amplitude anomalies and pockmarks.
- Trap failure is the most common cause of dry wells in basins worldwide. It is therefore important to quantify top-seal and fault-seal strength, and fault growth-history, as demonstrated by this study, to elucidate likely mechanisms and locations of hydrocarbon leakage. The approach seeks to reduce some of the inherent uncertainty associated with risking of the seal and improve estimations of feasible column heights that are used in reserve calculations.

Acknowledgements

We wish to thank DEA Norge AS for funding the PhD project resulting in this publication. Schlumberger is acknowledged for providing Petrel® for seismic interpretation and Techlog® for well log interpretation. Thanks to Badley Geoscience Ltd for providing the T7® software to perform fault seal analysis and for their reliable support. We are grateful to Bastian Wirth for his valuable insights into quantifying cap rock strength. Further thanks must been given to

Jostein Herredsvela for greatly improving the quality of the seismic data using de-noising and colour inversion techniques.

Funding

This research if fully funded by DEA Norge AS.

References

Allan, U.S. 1989. Model for hydrocarbon migration and entrapment within faulted structures. *AAPG bulletin*, **73**, 803-811.

Aydin, A. 2000. Fractures, faults, and hydrocarbon entrapment, migration and flow. *Marine and petroleum geology*, **17**, 797-814, https://doi.org/10.1016/S0264-8172(00)00020-9

Barton, C.A., Zoback, M.D. and Moos, D. 1995. Fluid flow along potentially active faults in crystalline rock. *Geology*, **23**, 683-686, https://doi.org/10.1130/0091-7613(1995)023<0683:FFAPAF>2.3.CO;2

Bastesen, E. and Rotevatn, A. 2012. Evolution and structural style of relay zones in layered limestone–shale sequences: insights from the Hammam Faraun Fault Block, Suez rift, Egypt. *Journal of the Geological Society*, **169,** 477-488, https://doi.org/10.1144/0016-76492011-100

Baudon, C. and Cartwright, J., 2008. The kinematics of reactivation of normal faults using high resolution throw mapping. *Journal of Structural Geology*, **30**, 1072-1084, https://doi.org/10.1016/j.jsg.2008.04.008

Bernal, A., 2009. Controls on economical hydrocarbon accumulations in the Askeladd Field, Barents Sea–A post-mortem fault seal analysis. *In: 2nd EAGE International Conference on Fault and Top Seals-From Pore to Basin Scale, Montpellier, France 21 - 24 September 2009*. European Association of Geoscientists and Engineers (EAGE), Houten, The Netherlands, https://doi.org/10.3997/2214-4609.20147192

Bhuyan, K. and Passey, Q.R., 1994. Clay estimation from GR and neutron-density porosity logs. *In*: *SPWLA 35th Annual Logging Symposium, Tulsa, Oklahoma 19-22 June 1994*. Society of Petrophysicists and Well-Log Analysts, Houston, Texas.

Bjørkum, P.A., Walderhaug, O. and Nadeau, P.H. 1998. Physical constraints on hydrocarbon leakage and trapping revisited. *Petroleum Geoscience*, **4**, 237-239, https://doi.org/10.1144/petgeo.4.3.237

Brandes, C., Polom, U. and Winsemann, J. 2011. Reactivation of basement faults: interplay of ice-sheet advance, glacial lake formation and sediment loading. *Basin Research*, **23**, 53-64, https://doi.org/10.1111/j.1365-2117-2010.00468.x

Bretan, P., Yielding, G. and Jones, H. 2003. Using calibrated shale gouge ratio to estimate hydrocarbon column heights. *AAPG bulletin*, **87**, 397-413, https://doi.org/10.1306/08010201128

Bretan, P. 2017. Trap Analysis: an automated approach for deriving column height predictions in fault-bounded traps. *Petroleum Geoscience*, **23**, 56-69, https://doi.org/10.1144/10.44petgeo2016-022

Caine, J.S., Evans, J.P. and Forster, C.B. 1996. Fault zone architecture and permeability structure. *Geology*, **24**, 1025-1028, https://doi.org/10.1130/0091-7613(1996)024<1025:FZAAPS>2.3.CO;2

Cartwright, J.A., Trudgill, B.D. and Mansfield, C.S. 1995. Fault growth by segment linkage: an explanation for scatter in maximum displacement and trace length data from the Canyonlands Grabens of SE Utah. *Journal of Structural Geology*, **17**, 1319-1326, https://doi.org/10.1016/0191-8141(95)00033-A

Cartwright, J., Huuse, M. and Aplin, A. 2007. Seal bypass systems. *AAPG bulletin*, **91**, 1141-1166, https://doi.org/10.1306/04090705181

Cavanagh, A.J., Di Primio, R., Scheck-Wenderoth, M. and Horsfield, B. 2006. Severity and timing of Cenozoic exhumation in the southwestern Barents Sea. *Journal of the Geological Society*, **163**, 761-774, https://doi.org/10.1144/0016-76492005-146

Cavanagh, A. and Wildgust, N. 2011. Pressurization and brine displacement issues for deep saline formation CO2 storage. *Energy Procedia*, **4**, 4814-4821, https://doi.org/10.1016/j.egypro.2011.02.447

Chand, S., Thorsnes, T., Rise, L., Brunstad, H., Stoddart, D., Bøe, R., Lågstad, P. and Svolsbru, T. 2012. Multiple episodes of fluid flow in the SW Barents Sea (Loppa High) evidenced by gas flares, pockmarks and gas hydrate accumulation. *Earth and Planetary Science Letters*, **331**, 305-314, https://doi.org/10.1016/j.epsl.2012.03.021

Childs, C., Walsh, J.J. and Watterson, J. 1997. Complexity in fault zone structure and implications for fault seal prediction. *In*: *Norwegian Petroleum Society Special Publications*, **7**, 61-72, https://doi.org/10.1016/S0928-8937(97)80007-0

Corcoran, D.V. and Doré, A.G. 2002. Top seal assessment in exhumed basin settings - Some insights from Atlantic margin and borderland basins. *In*: *Norwegian Petroleum Society Special Publications*, **11**, 89-107, https://doi.org/10.1016/S0928-8937(02)80009-1

Davatzes, N.C. and Hickman, S. 2005. Controls on fault-hosted fluid flow: Preliminary results from the Coso Geothermal Field, CA. *Geothermal Resources Council Transactions*, **29**, 343-348.

Demirmen, F. 2007. Reserves estimation: the challenge for the industry. *Journal of Petroleum Technology*, **59**, 80-89, https://doi.org/10.2118/103434-JPT

Dewhurst, D.N. and Yielding, G., 2017. Introduction to the thematic set: Fault and top seals. *In: 4th EAGE International Conference on Fault and Top Seals-From Pore to Basin Scale,* *Almeria, Spain 20 - 24 September 2015*. European Association of Geoscientists and Engineers (EAGE), Houten, The Netherlands, https://doi.org/10.1144/petgeo2016-303

Dimmen, V., Rotevatn, A., Peacock, D.C., Nixon, C.W. and Nærland, K. 2017. Quantifying structural controls on fluid flow: Insights from carbonate-hosted fault damage zones on the Maltese Islands. *Journal of Structural Geology*, **101**, 43-57, https://doi.org/10.1016/j.jsg.2017.05.012

Dolson, J. 2016. *Understanding oil and gas shows and seals in the search for hydrocarbons*. Springer.

Doré, A.G. 1995. Barents Sea geology, petroleum resources and commercial potential. *Arctic*, 207-221.

Doré, A.G. and Jensen, L.N. 1996. The impact of late Cenozoic uplift and erosion on hydrocarbon exploration: offshore Norway and some other uplifted basins. *Global and Planetary Change*, **12**, 415-436, https://doi.org/10.1016/0921-8181(95)00031-3

Doré, A.G. and Lundin, E.R. 1996. Cenozoic compressional structures on the NE Atlantic margin; nature, origin and potential significance for hydrocarbon exploration. *Petroleum Geoscience*, **2**, 299-311, https://doi.org/10.1144/petgeo.2.4.299

Doré, A.G., Cartwright, J.A., Stoker, M.S., Turner, J.P. and White, N.J. 2002. Exhumation of the North Atlantic margin: timing, mechanisms and implications for petroleum exploration. *Geological Society of London Special Publication*, **196**.

Downey, M. W. 1994. Hydrocarbon seal rocks, in L. B. Magoon and W. G. Dow, eds., The petroleum system: from source to trap: *AAPG Memoir*, **60**, 59–164

Duran, E.R., di Primio, R., Anka, Z., Stoddart, D. and Horsfield, B. 2013. 3D-basin modelling of the Hammerfest Basin (southwestern Barents Sea): A quantitative assessment of petroleum generation, migration and leakage. *Marine and petroleum geology*, **45**, 281-303, https://doi.org/10.1016/j.marpetgeo.2013.04.023

Færseth, R.B., Johnsen, E. and Sperrevik, S. 2007. Methodology for risking fault seal capacity: Implications of fault zone architecture. *AAPG bulletin*, **91**, 1231-1246, https://doi.org/10.1306/03080706051

Faleide, J.I., Gudlaugsson, S.T. and Jacquart, G. 1984. Evolution of the western Barents Sea. *Marine and Petroleum geology*, **1**, 123-150, https://doi.org/10.1016/0264-8172(84)90082-5

Faleide, J.I., Vågnes, E. and Gudlaugsson, S.T., 1993, January. Late Mesozoic–Cenozoic evolution of the southwestern Barents Sea. In *Geological Society, London, Petroleum Geology Conference series*, **4**, 933-950. Geological Society of London, https://doi.org/10.1144/0040933

Faleide, J.I., Tsikalas, F., Breivik, A.J., Mjelde, R., Ritzmann, O., Engen, O., Wilson, J. and Eldholm, O., 2008. Structure and evolution of the continental margin off Norway and the Barents Sea. *Episodes*, **31**, 82-91.

Faulkner, D.R., Jackson, C.A.L., Lunn, R.J., Schlische, R.W., Shipton, Z.K., Wibberley, C.A.J. and Withjack, M.O. 2010. A review of recent developments concerning the structure, mechanics and fluid flow properties of fault zones. *Journal of Structural Geology*, **32**, 1557-1575, https://doi.org/10.1016/j.jsg.2010.06.009

Fjeldskaar, W., Lindholm, C., Dehls, J.F. and Fjeldskaar, I. 2000. Postglacial uplift, neotectonics and seismicity in Fennoscandia. *Quaternary Science Reviews*, **19**, 1413-1422, https://doi.org/10.1016/S0277-3791(00)00070-6

Fossen, H. 2016. *Structural geology*. Cambridge University Press.

Fossen, H. and Rotevatn, A. 2016. Fault linkage and relay structures in extensional settings - A review. *Earth-Science Reviews*, **154**, 14-28, https://doi.org/10.1016/j.earscirev.2015.11.014

Fredman, N., Tveranger, J., Semshaug, S., Braathen, A. and Sverdrup, E. 2007. Sensitivity of fluid flow to fault core architecture and petrophysical properties of fault rocks in siliciclastic reservoirs: a synthetic fault model study. *Petroleum Geoscience*, **13**, 305-320, https://doi.org/10.1144/1354-079306-721

Gabrielsen, R.H. 1984. Long-lived fault zones and their influence on the tectonic development of the southwestern Barents Sea. *Journal of the Geological Society*, **141**, 651-662, https://doi.org/10.1144/gsjgs.141.4.0651

Gabrielsen, R.H., Faerseth, R.B. and Jensen, L.N. 1990. *Structural elements of the Norwegian continental shelf. Part. 1. The Barents Sea region*. Norwegian Petroleum Directorate.

Gabrielsen, R.H. and Kløvjan, O.S. 1997. Late Jurassic—early Cretaceous caprocks of the southwestern Barents Sea: fracture systems and rock mechanical properties. In *Norwegian Petroleum Society Special Publications*, **7**, 73-89), https://doi.org/10.1016/S0928-8937(97)80008-2

Gabrielsen, R.H., Grunnaleite, I. and Rasmussen, E. 1997. Cretaceous and tertiary inversion in the Bjørnøyrenna Fault Complex, south-western Barents Sea. *Marine and Petroleum Geology*, **14**,165-178, https://doi.org/10.1016/S0264-8172(96)00064-5

Gartrell, A., Zhang, Y., Lisk, M. and Dewhurst, D. 2004. Fault intersections as critical hydrocarbon leakage zones: integrated field study and numerical modelling of an example from the Timor Sea, Australia. *Marine and petroleum geology*, **21**, 1165-1179, https://doi.org/10.1016/j.marpetgeo.2004.08.001

Grollimund, B. and Zoback, M.D. 2003. Impact of glacially induced stress changes on fault-seal integrity offshore Norway. *AAPG bulletin*, **87**, 493-506, https://doi.org/10.1306/08010401134

Grunau, H.R. 1987. A worldwide look at the cap-rock problem. *Journal of Petroleum Geology*, **10**, 245-265, https://doi.org/10.1111/j.1747-5457.1987.tb00945.x

Gudlaugsson, S.T., Faleide, J.I., Johansen, S.E. and Breivik, A.J. 1998. Late Palaeozoic structural development of the south-western Barents Sea. *Marine and Petroleum Geology*, ***15***, 73-102, https://doi.org/10.1016/S0264-8172(97)00048-2

Heggland, R. 2005. Using gas chimneys in seal integrity analysis: A discussion based on case histories, *in P. Boult and J. Kaldi, eds., Evaluating fault and cap rock seals: AAPG Hedberg Series*, **2**, 237-245, https://doi.org/10.1306/1060767H23170

Henriksen, E., Ryseth, A.E., Larssen, G.B., Heide, T., Rønning, K., Sollid, K. and Stoupakova, A.V. 2011. Tectonostratigraphy of the greater Barents Sea: implications for petroleum systems. *Geological Society, London, Memoirs*, **35**, 163-195, https://doi.org/10.1144/M35.10

Hermanrud, C., Halkjelsvik, M.E., Kristiansen, K., Bernal, A. and Strömbäck, A.C. 2014. Petroleum column-height controls in the western Hammerfest Basin, Barents Sea. *Petroleum Geoscience*, **20**, 227-240, https://doi.org/10.1144/petgeo2013-041

Ibrahim, MA, Tek, MR, Katz, DL. 1970. Threshold pressure in gas storage. *Pipeline Research Committee American*. Gas Association at the University of Michigan, Michigan.

Ingram, G.M. and Urai, J.L. 1999. Top-seal leakage through faults and fractures: the role of mudrock properties. *Geological Society, London, Special Publications*, **158,** 125-135, https://doi.org/10.1144/GSL.SP.1999.158.01.10

Jackson, C.A.L. and Rotevatn, A. 2013. 3D seismic analysis of the structure and evolution of a salt-influenced normal fault zone: a test of competing fault growth models. *Journal of Structural Geology*, **54**, 215-234, https://doi.org/10.1016/j.jsg.2013.06.012

Johansen, S.E., Ostisty, B.K., Fedorovsky, Y.F., Martirosjan, V.N., Christensen, O.B., Cheredeev, S.I., Ignatenko, E.A. and Margulis, L.S. 1993. Hydrocarbon potential in the Barents Sea region: play distribution and potential. *In: Norwegian Petroleum Society Special Publications*, **2**, 273-320, https://doi.org/10.1016/B978-0-444-88943-0.50024-1

Kearey, P., Brooks, M. and Hill, I. 2013. *An introduction to geophysical exploration*. John Wiley & Sons.

Knipe, R. J. 1993. The influence of fault zone processes and diagenesis on fluid flow, in A. D.Horbury and . G.Robinson, eds., *Diagenesis and basin development: AAPG Studies in Geology*, **36**, chapter 10, 135–151.

Knipe, R.J. 1997. Juxtaposition and seal diagrams to help analyze fault seals in hydrocarbon reservoirs. *AAPG bulletin*, **81**, 187-195.

Knipe, R.J., Fisher, Q.J., Jones, G., Clennell, M.R., Farmer, A.B., Harrison, A., Kidd, B., McAllister, E., Porter, J.R. and White, E.A. 1997. Fault seal analysis: successful methodologies, application and future directions. *In: Norwegian Petroleum Society Special Publications*, **7**, 15-38, https://doi.org/10.1016/S0928-8937(97)80004-5

Larsen, R.M., Fjaeran, T. and Skarpnes, O. 1993. Hydrocarbon potential of the Norwegian Barents Sea based on recent well results. *In: Norwegian Petroleum Society Special Publications*, **2**, 321-331, https://doi.org/10.1016/B978-0-444-88943-0.50025-3

Lerch, B., Karlsen, D.A., Matapour, Z., Seland, R. and Backer-Owe, K. 2016. Organic geochemistry of Barents Sea petroleum: thermal maturity and alteration and mixing processes in oils and condensates. *Journal of Petroleum Geology*, **39**, 125-148, https://doi.org/10.1111/jpg.12637

Lundin, E. and Doré, A.G. 2002. Mid-Cenozoic post-breakup deformation in the ‘passive’margins bordering the Norwegian–Greenland Sea. *Marine and Petroleum Geology*, **19**, 79-93, https://doi.org/10.1016/S0264-8172(01)00046-0

Makurat, A., Torudbakken, B., Monsen, K. and Rawlings, C. 1992, January. Cenezoic uplift and caprock seal in the Barents Sea: fracture modelling and seal risk evaluation. *In: SPE Annual Technical Conference and Exhibition, Washington, D.C 4-7 October*. Society of Petroleum Engineers (SPE), Richardson, Texas, https://doi.org/10.2118/24740-MS

Mohammedyasin, S.M., Lippard, S.J., Omosanya, K.O., Johansen, S.E. and Harishidayat, D. 2016. Deep-seated faults and hydrocarbon leakage in the Snøhvit Gas Field, Hammerfest Basin, southwestern Barents Sea. *Marine and Petroleum Geology*, **77**, 160-178, https://doi.org/10.1016/j.marpetgeo.2016.06.011

Moretti, I. 1998. The role of faults in hydrocarbon migration. *Petroleum Geoscience*, **4**, 81-94, https://doi.org/10.1144/petgeo.4.1.81

NPD. 2018. Resource Report Exploration 2018. Norwegian Petroleum Directorate (NPD), Stavanger, Norway, http://www. npd.no/en/Publications [last accessed June 2019].

Nyland, B., Jensen, L.N., Skagen, J.L., Skarpnes, O. and Vorren, T. 1992. Tertiary uplift and erosion in the Barents Sea: magnitude, timing and consequences. *In: Structural and tectonic modelling and its application to Petroleum Geology (Eds. R.M. Larsen et al.), Norwegian Petroleum Society Special Publication*, **1**, 153-162, https://doi.org/10.1016/B978-0-444-88607-1.50015-2

Ohm, S.E., Karlsen, D.A. and Austin, T.J.F. 2008. Geochemically driven exploration models in uplifted areas: Examples from the Norwegian Barents Sea. *AAPG bulletin*, **92**, 1191-1223, https://doi.org/10.1306/06180808028

Ostanin, I., Anka, Z., di Primio, R. and Bernal, A. 2012. Identification of a large Upper Cretaceous polygonal fault network in the Hammerfest basin: Implications on the reactivation of regional faulting and gas leakage dynamics, SW Barents Sea. *Marine Geology*, **332**, 109-125. https://doi.org/10.1016/j.margeo.2012.03.005

Ostanin, I., Anka, Z., di Primio, R. and Bernal, A. 2013. Hydrocarbon plumbing systems above the Snøhvit gas field: structural control and implications for thermogenic methane leakage in the Hammerfest Basin, SW Barents Sea. *Marine and Petroleum Geology*, **43**, 127-146, https://doi.org/10.1016/j.marpetgeo.2013.02.012

Ostanin, I., Anka, Z. and di Primio, R. 2017. Role of Faults in Hydrocarbon Leakage in the Hammerfest Basin, SW Barents Sea: Insights from Seismic Data and Numerical Modelling. *Geosciences*, **7**, 28, https://doi.org/10.3390/geosciences7020028

Peacock, D.C.P. and Sanderson, D.J. 1991. Displacements, segment linkage and relay ramps in normal fault zones. *Journal of Structural Geology*, **13**, 721-733, https://doi.org/10.1016/0191-8141(91)90033-F

Poelchau, H.S., Baker, D.R., Hantschel, Th., Horsfield, B., Wygrala, B. 1997. *Basin simulation and the design of the conceptual basin model. In: Welte, D.H., Horsfield B., Baker, D.R. (Eds.), Petroleum and Basin Evolution.* Springer, Berlin, 3–70.

Rider, M. and Kennedy, M. 2011. *The Geological Interpretation of Well Logs*. Published by Rider-French Consulting Ltd, 3rd Edition, Bell and Bain, Glasgow.

Rodrigues, E., di Primio, R., Anka, Z., Stoddart, D. and Horsfield, B. 2011. Leakage of hydrocarbons in a glacially influenced marine environment: Hammerfest Basin (Southwestern Barents Sea.). *In: Geophysical Research Abstracts*, **13.**

Rotevatn, A., Sandve, T.H., Keilegavlen, E., Kolyukhin, D. and Fossen, H. 2013. Deformation bands and their impact on fluid flow in sandstone reservoirs: the role of natural thickness variations. *Geofluids*, **13**, 359-371, https://doi.org/10.1111/gfl.12030

Rotevatn, A. and Jackson, C.A.L. 2014. 3D structure and evolution of folds during normal fault dip linkage. *Journal of the Geological Society*, **171**, 821-829, https://doi.org/10.1144/jgs2014-045

Rudolph, K.W. and Goulding, F.J. 2017. Benchmarking exploration predictions and performance using 20+ yr of drilling results: One company’s experience. *AAPG Bulletin*, **101**, 161-176, https://doi.org/10.1306/06281616060

Sanderson, D.J. and Nixon, C.W. 2015. The use of topology in fracture network characterization. *Journal of Structural Geology*, **72,** 55-66, https://doi.org/10.1016/j.jsg.2015.01.005

Schlömer, S. and Krooss, B.M. 1997. Experimental characterisation of the hydrocarbon sealing efficiency of cap rocks. *Marine and Petroleum Geology*, **14**, 565-580, https://doi.org/10.1016/S0264-8172(97)00022-6

Simm, R., Bacon, M. and Bacon, M. 2014. *Seismic Amplitude: An interpreter's handbook*. Cambridge University Press.

Simmenes, T.H., Hermanrud, C., Ersland, R., Georgescu, L. and Sollie, O.C.E. 2017. Relationships between bright amplitudes in overburden rocks and leakage from underlying reservoirs on the Norwegian Continental Shelf. *Petroleum Geoscience*, **23**, 10-16, https://doi.org/10.1144/petgeo2016-093

Sperrevik, S., Gillespie, P.A., Fisher, Q.J., Halvorsen, T. and Knipe, R.J. 2002. Empirical estimation of fault rock properties. *In: Norwegian Petroleum Society Special Publications*, **11**, 109-125, https://doi.org/10.1016/S0928-8937(02)80010-8

Tamagawa, T. and Pollard, D.D. 2008. Fracture permeability created by perturbed stress fields around active faults in a fractured basement reservoir. *AAPG bulletin*, **92**, 743-764, https://doi.org/10.1306/02050807013

Tvedt, A.B., Rotevatn, A., Jackson, C.A.L., Fossen, H. and Gawthorpe, R.L. 2013. Growth of normal faults in multilayer sequences: A 3D seismic case study from the Egersund Basin, Norwegian North Sea. *Journal of Structural Geology*, **55**, 1-20, https://doi.org/10.1016/j.jsg.2013.08.002

Vassenden, F., Sylta, Ø. and Zwach, C. 2003. Secondary Migration in a 2D Visual Laboratory Model. *In Fault and Top Seals: What do we know and where do we go?* EAGE Fault and Top Seal meeting, Montpellier, France, 8-11 September

Watts, N.L. 1987. Theoretical aspects of cap-rock and fault seals for single-and two-phase hydrocarbon columns. *Marine and Petroleum Geology*, **4**, 274-307, https://doi.org/10.1016/0264-8172(87)90008-0

Wibberley, C.A., Gonzalez-Dunia, J. and Billon, O. 2017. Faults as barriers or channels to production-related flow: insights from case studies. *Petroleum Geoscience*, **23**, 134-147, https://doi.org/10.1144/petgeo2016-057

Wiprut, D. and Zoback, M.D. 2002. Fault reactivation, leakage potential, and hydrocarbon column heights in the northern North Sea. In *Norwegian Petroleum Society Special Publications*, **11**, 203-219, https://doi.org/10.1016/S0928-8937(02)80016-9

Yielding, G., Freeman, B. and Needham, D.T. 1997. Quantitative fault seal prediction. *AAPG bulletin*, **81**, 897-917.

Yielding, G. 2002. Shale gouge ratio - Calibration by geohistory. *In: Norwegian Petroleum Society Special Publications*, **11**, 1-15, https://doi.org/10.1016/S0928-8937(02)80003-0

Yielding, G., Bretan, P. and Freeman, B. 2010. Fault seal calibration: a brief review. *Geological Society, London, Special Publications*, **347**, 243-255, https://doi.org/10.1144/SP347.14

Zhang, Y., Schaubs, P.M., Zhao, C., Ord, A., Hobbs, B.E. and Barnicoat, A.C. 2008. Fault-related dilation, permeability enhancement, fluid flow and mineral precipitation patterns: numerical models. *Geological Society, London, Special Publications*, **299**, 239-255, https://doi.org/10.1144/SP299.15

Zieglar, D.L. 1992. Hydrocarbon Columns, Buoyancy Pressures, and Seal Efficiency: Comparisons of Oil and Gas Accumulations in California and the Rocky Mountain Area (1). *AAPG Bulletin*, **76**, 501-508.

Table 1. Inputs used in TrapTester to model the fault-seal strength of the faults that define each structure and to ascertain the corresponding maximum gas column height that can be supported.

Structure	No. of fault elements	Well used for Vclay input	Uplift correction (m)	Hydrocarbon density (kg/m^3)	Water density (kg/m^3)
Snøhvit Nord	2	7121/4-2	1000	205	1110
Snøhvit central	5	7120/6-1, 7120/6-2S, 7121/4-1, 7121/5-1	1000	205	1121
Albatross (south)	2	7121/7-2, 7120/9-1, 7121/7-2	1000	176	1059
Askeladd (north)	4	7120/8-1, 7120/8-2	750	182	1040
Askeladd (south)	3	7120/8-1, 7120/8-2	750	182	1040

Figure captions

Fig. 1. A schematic showing a fault-bounded trap that relies on top and lateral seal. The measurements required to calculate the discovered hydrocarbon column height, the trap height and the overburden are marked.

Fig. 2. The SW Barents Sea with major structural elements and location of the seismic data covering the majority of hydrocarbon fields that constitute the Snøhvit field. Modified after Cavanagh et al. (2006)**.**

Fig. 3. Tectonostratigraphic chart that indicates the major source rocks and reservoirs, and major structural events across the SW Barents Sea.

Fig. 4. Depth map of the top Stø formation limited by the fluid contact depth for each structure. The bars refer to the column of hydrocarbons and water with shows discovered in each borehole. Major faults are shown in black.

Fig. 5. A bar graph of measured and calculated hydrocarbon column heights for each structure. The light blue bar is the theoretical column that can be supported by the faults based on fault seal analysis. The medium blue bar represents the trap height and the dark blue bar represents the actual hydrocarbon column height.

Fig. 6. The map shows the top Stø surface in depth. White polygons indicate the areal extent of each individual structure down to the discovered fluid contact. The location of the five cross sections is indicated on the map. Cross sections are shown for Snøhvit Nord structure (A-A'), the Snøhvit central structure (B-B'), the Albatross south structure (C-C'), the Askeladd north structure (D-D'), and the Askeladd south structure (E-E') with the depths of the actual fluid contact, modelled fault-sealed fluid contact, deepest show, spill depth and top reservoir.

Fig. 7. Figure (**a**) shows the empirical relationship between porosity and depth according to different shale porosities. Petrophysical measurements for the Hekkingen cap rock are marked on the graph showing it is a low porosity/tight seal. Figure (**b**) shows the empirical relationship between threshold pressure with depth, based on laboratory testing of core samples. The low porosity/tight seal curves are in bold. Modified from Cavanagh and Wildgust (2011).

Fig. 8. The results of four theoretical hydrocarbon column heights based on top seal properties versus actual column heights measured across the Hammerfest Basin.

Fig. 9. Three different examples of a series of T-z plots whereby the throw (m) is plotted against increasing depth/age at consistent intervals along each fault. Individual insert maps show the location of the fault. Each fault profile represents the three major fault slip histories recorded across the Snøhvit field.

Fig. 10. Schematic illustration of different styles of fault evolution observed in the T-z plots beginning with t1, where t is time. Syn-sedimentary faulting results in an asymmetric T-z profile due to the presence of a free surface. The fault is then buried (t2). If no further throw is observed, it is a category 3 fault. Post-sedimentary faulting occurs in two different ways. In scenario a, the fault is reactivated by blind propagation (t3) resulting in a gradual decrease of the fault throw. This is characteristic of category 2 faults. In scenario b at t2, a smaller fault nucleates in the overburden and after some time (t3), links vertically with the deeper fault resulting in two throw maxima. This is characteristic of category 1 faults. Modified after Tvedt et al. (2013).

Fig. 11. A map showing key faults that define the six structures in the Snøhvit gas field, which have been categorized according to their fault-growth history.

Fig. 12. The base map of the Stø (Middle Jurassic) formation with major faults highlighted. Bright red areas represent high values of the RMS amplitude attribute taken across a window over the Kveite (Late Cretaceous) formation. The bright amplitudes located along the two cross sections are circled in yellow and also displayed in 3D view in the final panel. Cross section A-A' partially covers the Askeladd North structure and cross-section B-B' partially covers the Snøhvit central structure.

Fig. 13. A summary of locations and mechanisms of hydrocarbon leakage in a fault-bounded trap. Unlikely mechanisms are capillary breach across the cap rock and fault, and mechanical failure of the cap rock. The likely mechanism is top-seal breach caused by fault reactivation and dilation.

Figures

Figure 1

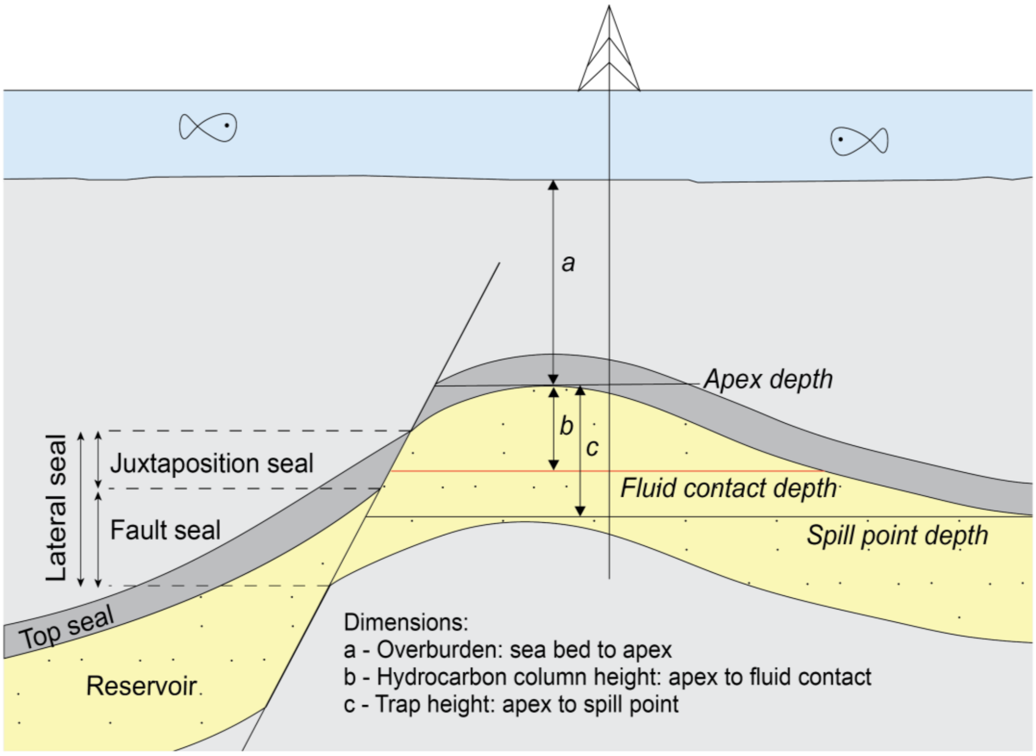

Figure 2

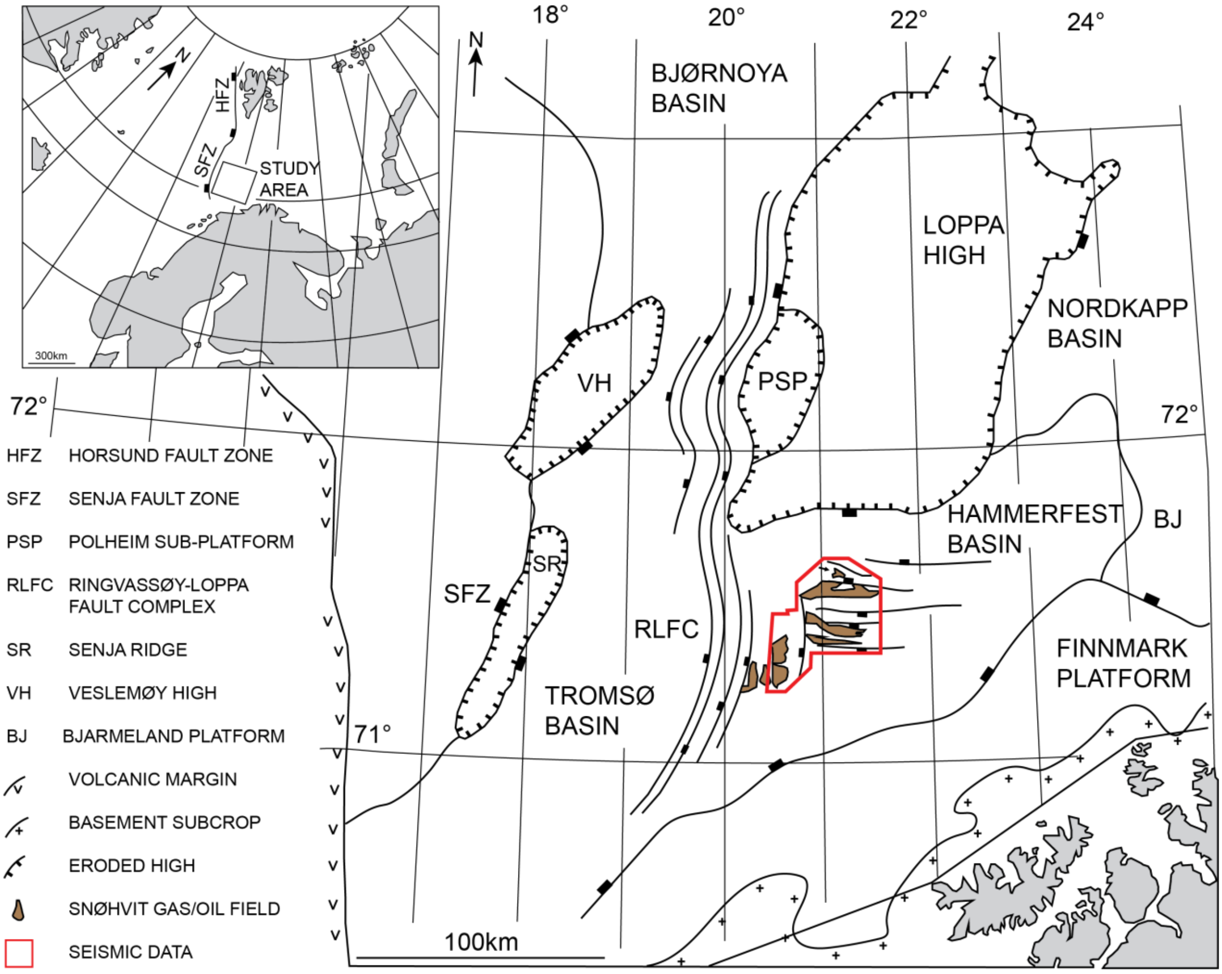

N
HFZ
SFZ
STUDY AREA
300km
18°
20°
22°
24°
BJØRNOYA BASIN
LOPPA HIGH
NORDKAPP BASIN
VH
PSP
72°
72°
HAMMERFEST BASIN
BJ
SR
SFZ
RLFC
TROMSØ BASIN
FINNMARK PLATFORM
71°
100km
HFZ HORSUND FAULT ZONE
SFZ SENJA FAULT ZONE
PSP POLHEIM SUB-PLATFORM
RLFC RINGVASSØY-LOPPA FAULT COMPLEX
SR SENJA RIDGE
VH VESLEMØY HIGH
BJ BJARMELAND PLATFORM
VOLCANIC MARGIN
BASEMENT SUBCROP
ERODED HIGH
SNØHVIT GAS/OIL FIELD
SEISMIC DATA

Figure 3

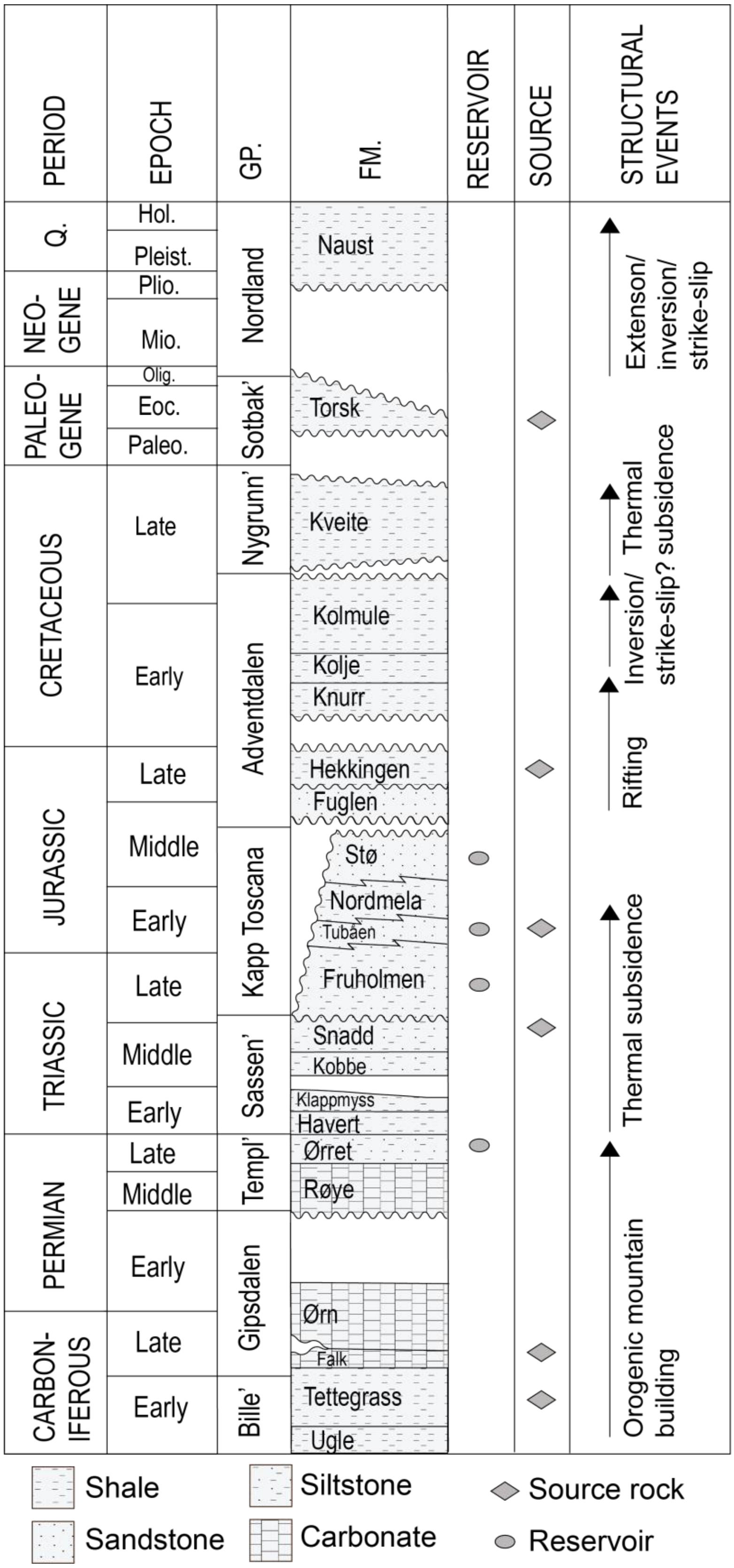

PERIOD
EPOCH
GP.
FM.
RESERVOIR
SOURCE
STRUCTURAL EVENTS
Q.
NEO-GENE
PALEO-GENE
CRETACEOUS
JURASSIC
TRIASSIC
PERMIAN
CARBON-IFEROUS
Hol.
Pleist.
Plio.
Mio.
Olig.
Eoc.
Paleo.
Late
Early
Late
Middle
Early
Late
Middle
Early
Late
Middle
Early
Late
Early
Nordland
Sotbak'
Nygrunn'
Adventdalen
Kapp Toscana
Sassen'
Templ'
Gipsdalen
Bille'
Naust
Torsk
Kveite
Kolmule
Kolje
Knurr
Hekkingen
Fuglen
Stø
Nordmela
Tubåen
Fruholmen
Snadd
Kobbe
Klappmyss
Havert
Ørret
Røye
Ørn
Falk
Tettegrass
Ugle
Extenson/ inversion/ strike-slip
Inversion/ strike-slip?
Thermal subsidence
Rifting
Thermal subsidence
Orogenic mountain building
Shale
Sandstone
Siltstone
Carbonate
Source rock
Reservoir

Figure 4

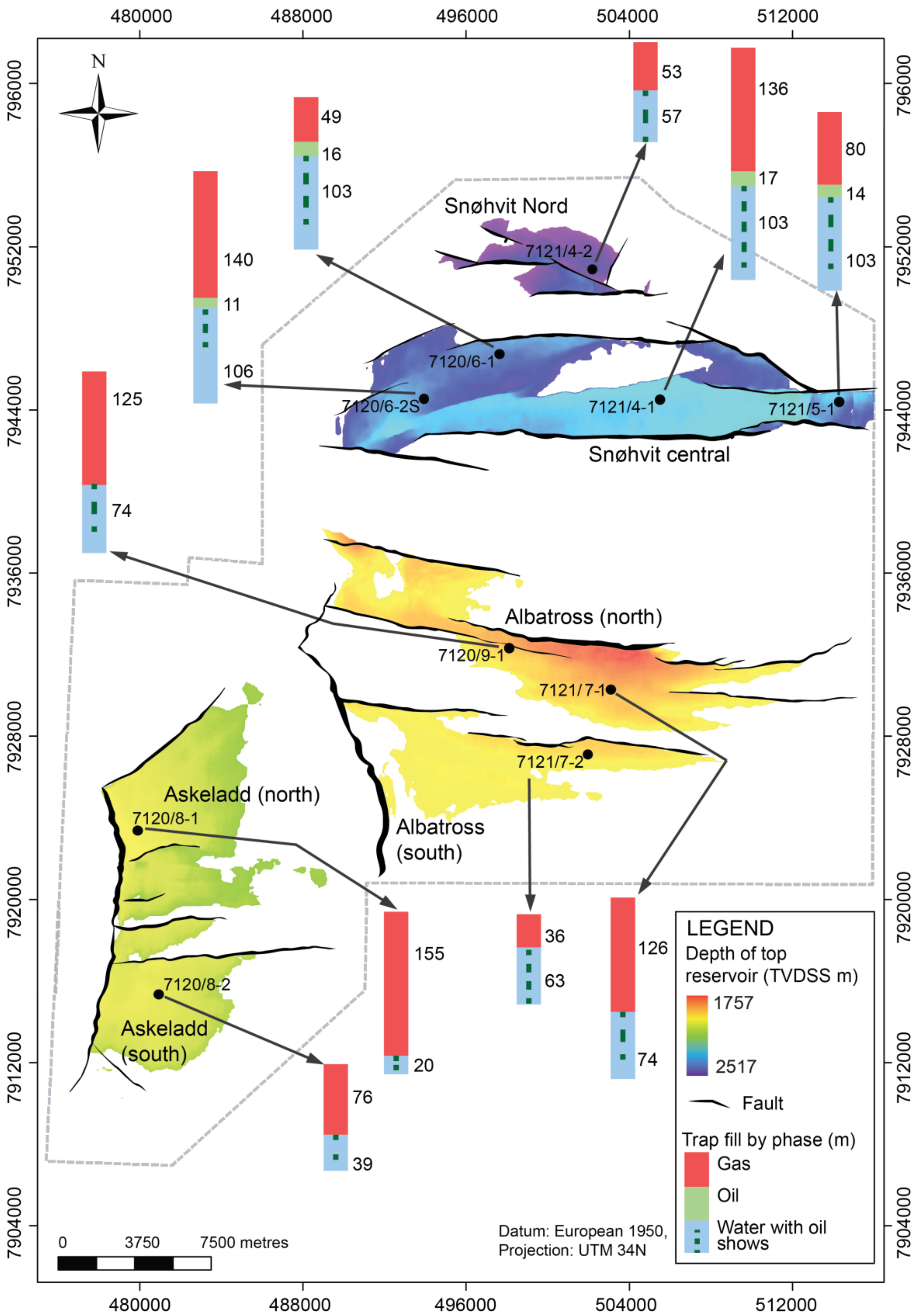

Snøhvit Nord
Snøhvit central
Albatross (north)
Albatross (south)
Askeladd (north)
Askeladd (south)
7121/4-2
7120/6-1
7120/6-2S
7121/4-1
7121/5-1
7120/9-1
7121/7-1
7121/7-2
7120/8-1
7120/8-2
LEGEND
Depth of top reservoir (TVDSS m)
1757
2517
Fault
Trap fill by phase (m)
Gas
Oil
Water with oil shows
Datum: European 1950, Projection: UTM 34N
0 3750 7500 metres

Figure 5

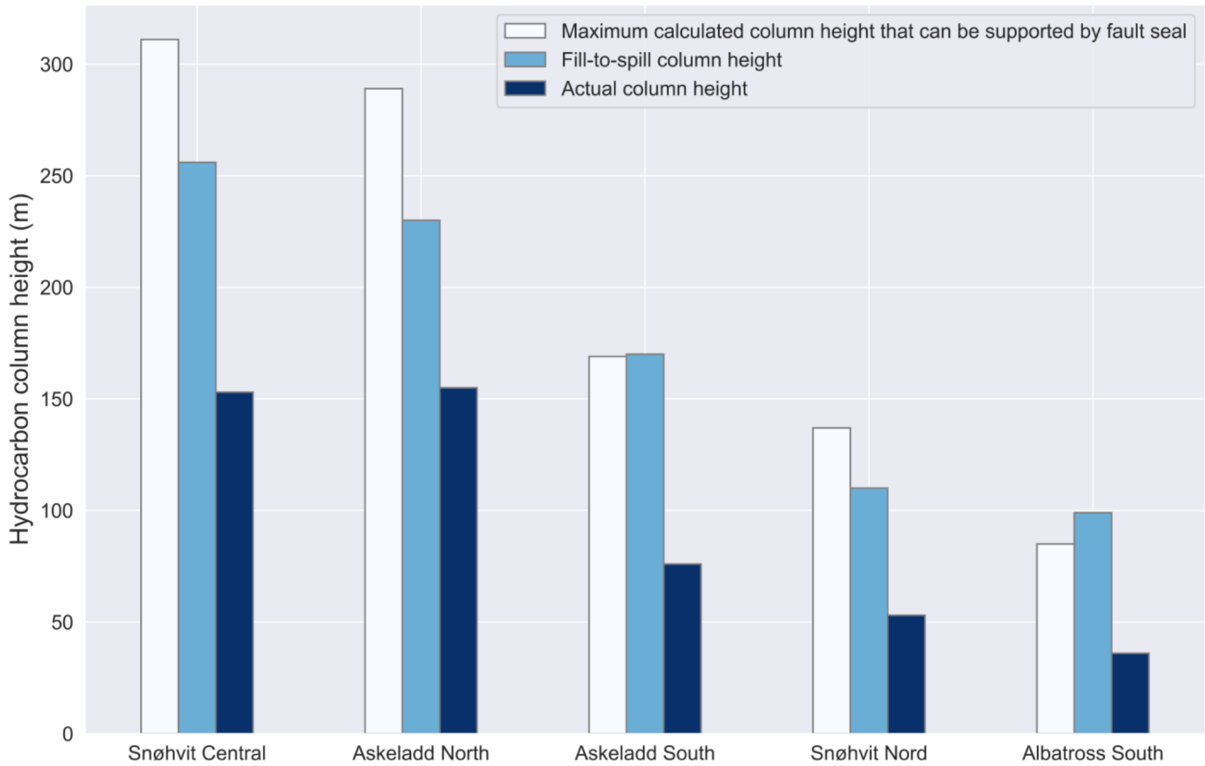
Maximum calculated column height that can be supported by fault seal
Fill-to-spill column height
Actual column height
Hydrocarbon column height (m)
300
250
200
150
100
50
0
Snøhvit Central
Askeladd North
Askeladd South
Snøhvit Nord
Albatross South

Figure 6

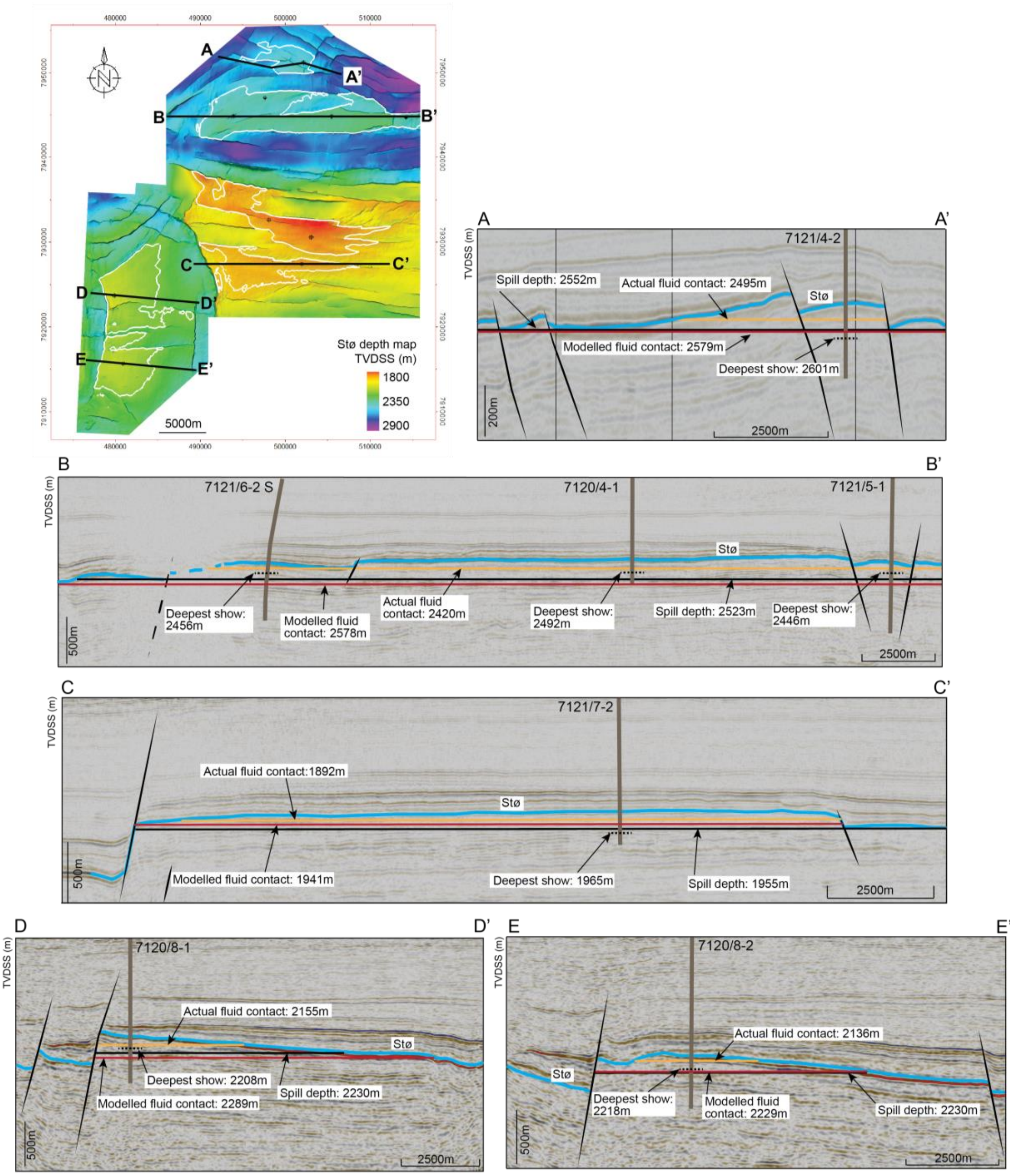

A
A'
B
B'
C
C'
D
D'
E
E'
Stø depth map
TVDSS (m)
1800
2350
2900
5000m
TVDSS (m)
7121/4-2
Spill depth: 2552m
Actual fluid contact: 2495m
Stø
Modelled fluid contact: 2579m
Deepest show: 2601m
200m
2500m
7121/6-2 S
7120/4-1
7121/5-1
Stø
Deepest show: 2456m
Modelled fluid contact: 2578m
Actual fluid contact: 2420m
Deepest show: 2492m
Spill depth: 2523m
Deepest show: 2446m
500m
2500m
7121/7-2
Actual fluid contact:1892m
Stø
Modelled fluid contact: 1941m
Deepest show: 1965m
Spill depth: 1955m
500m
2500m
7120/8-1
Actual fluid contact: 2155m
Stø
Deepest show: 2208m
Spill depth: 2230m
Modelled fluid contact: 2289m
500m
2500m
7120/8-2
Actual fluid contact: 2136m
Stø
Deepest show: 2218m
Modelled fluid contact: 2229m
Spill depth: 2230m
500m
2500m

Figure 7

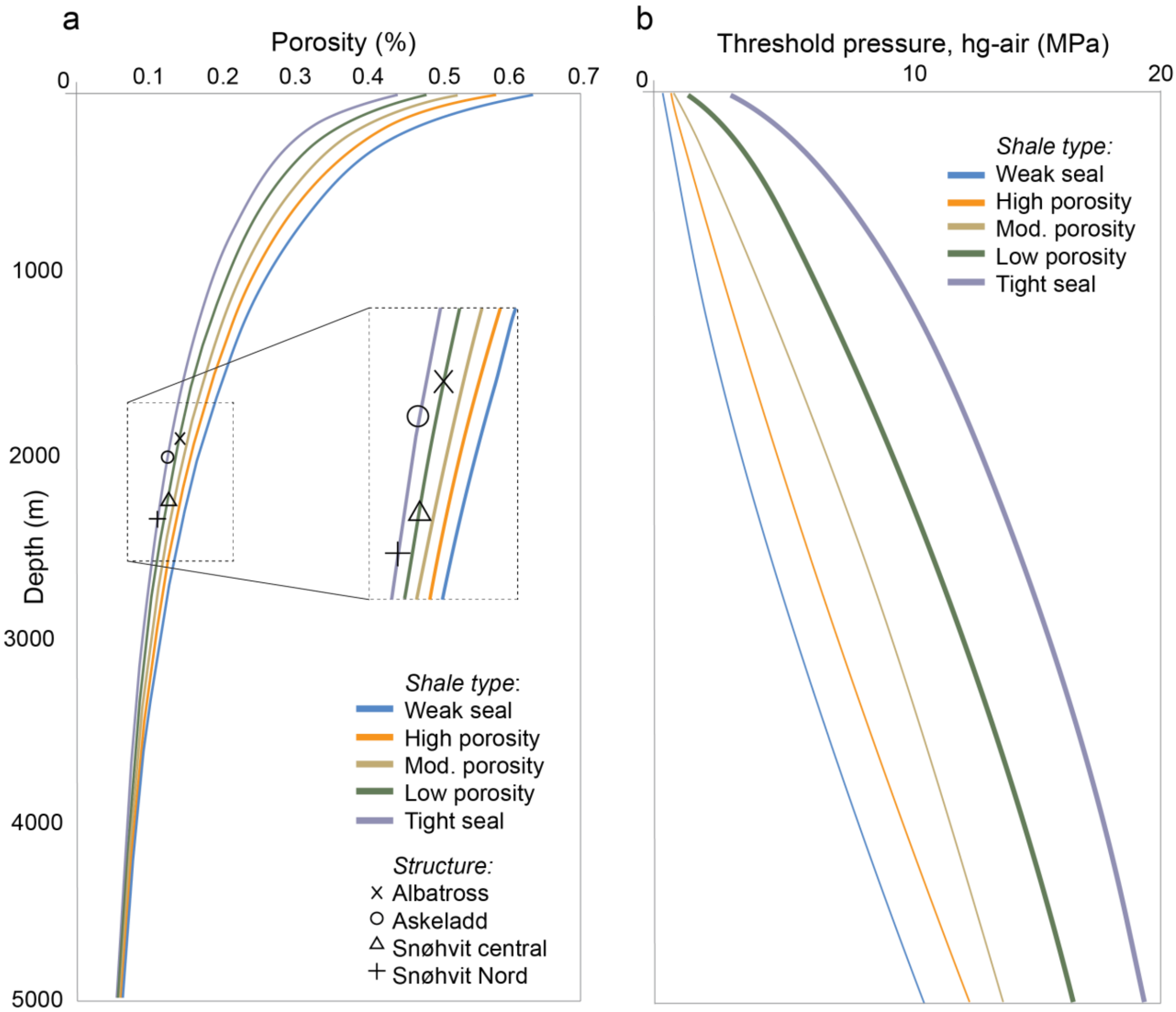

a
Porosity (%)
0
0.1
0.2
0.3
0.4
0.5
0.6
0.7
1000
2000
3000
4000
5000
Depth (m)
Shale type:
Weak seal
High porosity
Mod. porosity
Low porosity
Tight seal
Structure:
Albatross
Askeladd
Snøhvit central
Snøhvit Nord
b
Threshold pressure, hg-air (MPa)
0
10
20
Shale type:
Weak seal
High porosity
Mod. porosity
Low porosity
Tight seal

Figure 8

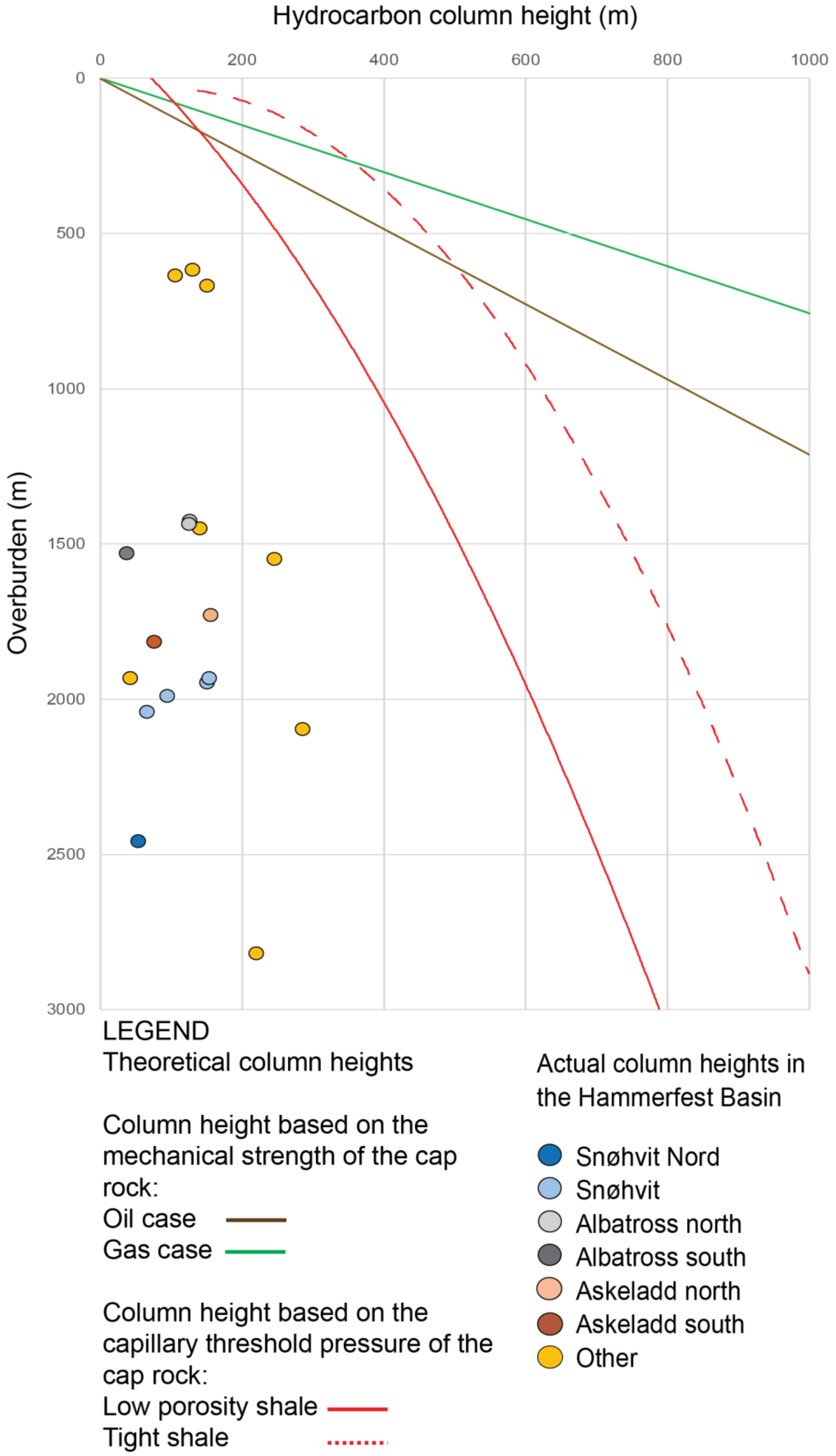
Hydrocarbon column height (m)
0
200
400
600
800
1000
0
500
1000
1500
2000
2500
3000
Overburden (m)
LEGEND
Theoretical column heights
Column height based on the mechanical strength of the cap rock:
Oil case
Gas case
Column height based on the capillary threshold pressure of the cap rock:
Low porosity shale
Tight shale
Actual column heights in the Hammerfest Basin
Snøhvit Nord
Snøhvit
Albatross north
Albatross south
Askeladd north
Askeladd south
Other

Figure 9

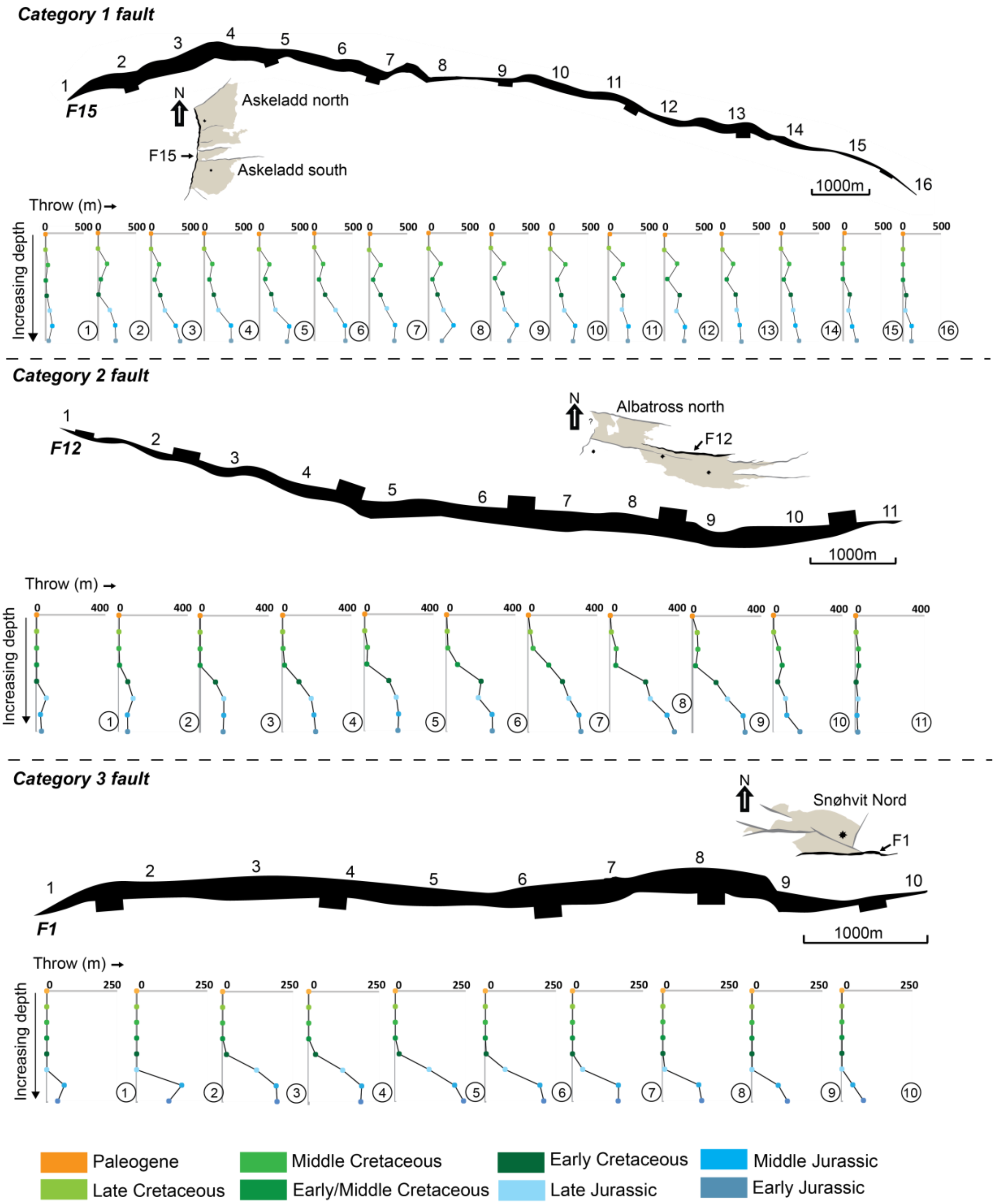

Category 1 fault
F15
Askeladd north
Askeladd south
N
1000m
Throw (m)
Increasing depth
Category 2 fault
F12
Albatross north
1000m
Throw (m)
Increasing depth
Category 3 fault
F1
Snøhvit Nord
1000m
Throw (m)
Increasing depth
Paleogene
Late Cretaceous
Middle Cretaceous
Early/Middle Cretaceous
Early Cretaceous
Late Jurassic
Middle Jurassic
Early Jurassic

Figure 10

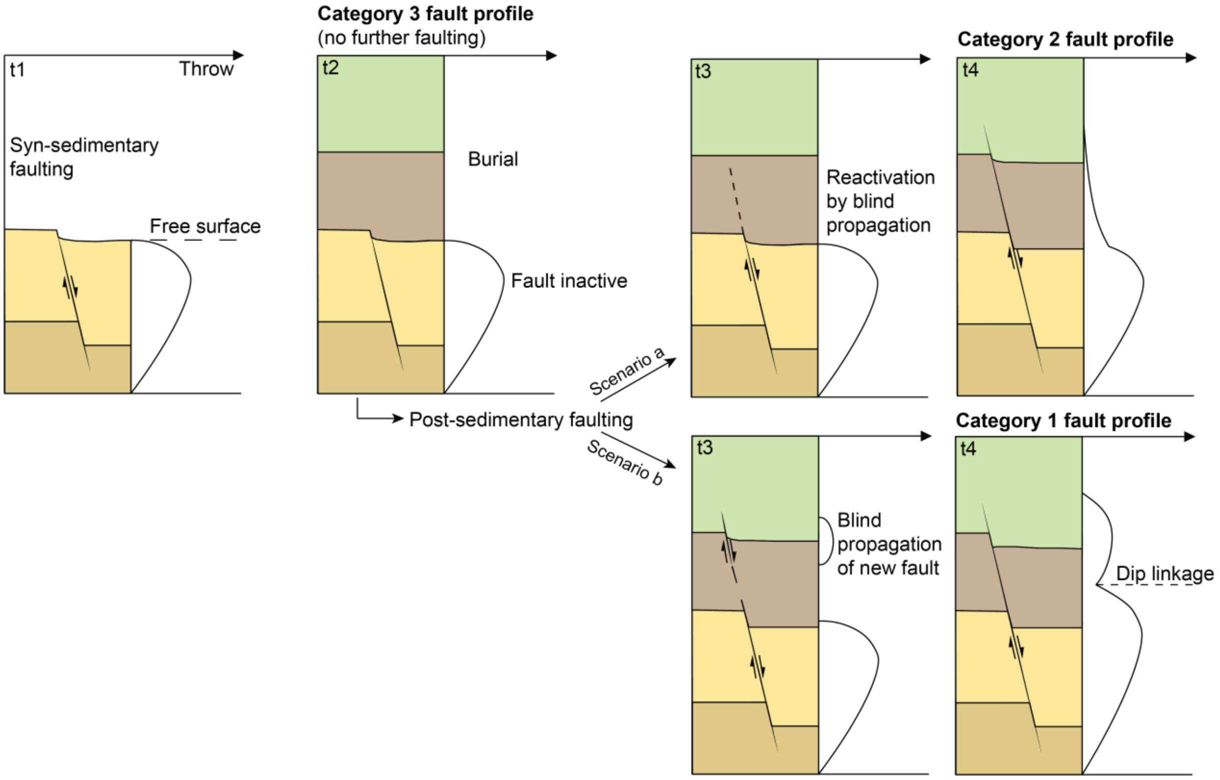
Category 3 fault profile
(no further faulting)
t1
Throw
Syn-sedimentary faulting
Free surface
t2
Burial
Fault inactive
Post-sedimentary faulting
Scenario a
Scenario b
t3
Reactivation by blind propagation
Category 2 fault profile
t4
t3
Blind propagation of new fault
Category 1 fault profile
t4
Dip linkage

Figure 11

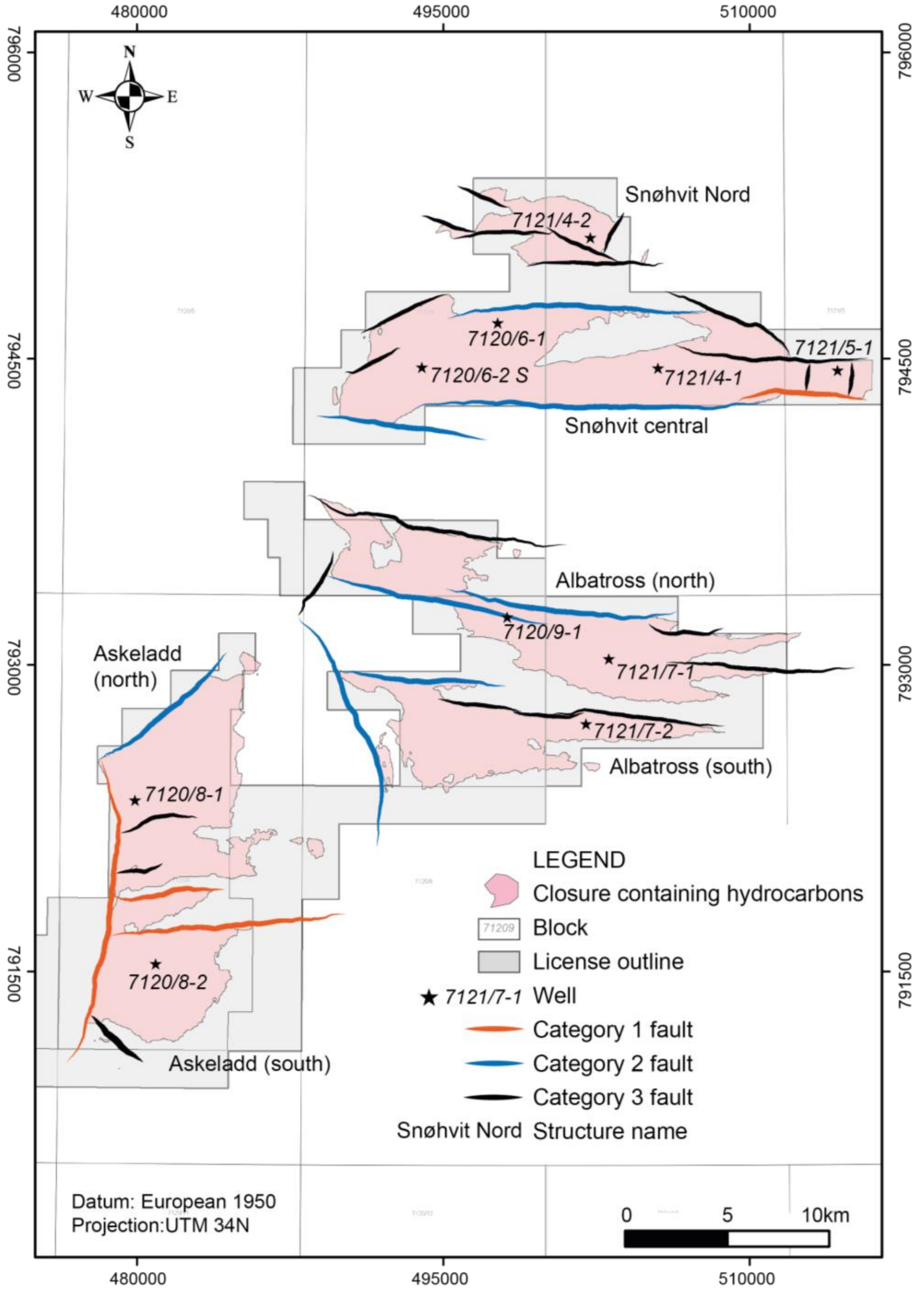
480000
495000
510000
796000
794500
793000
791500
N
S
W
E
Snøhvit Nord
7121/4-2
7120/6-1
7120/6-2 S
7121/4-1
7121/5-1
Snøhvit central
Albatross (north)
7120/9-1
7121/7-1
7121/7-2
Albatross (south)
Askeladd (north)
7120/8-1
7120/8-2
Askeladd (south)
LEGEND
Closure containing hydrocarbons
71209
Block
License outline
7121/7-1 Well
Category 1 fault
Category 2 fault
Category 3 fault
Snøhvit Nord Structure name
Datum: European 1950
Projection:UTM 34N
0
5
10km

Figure 12

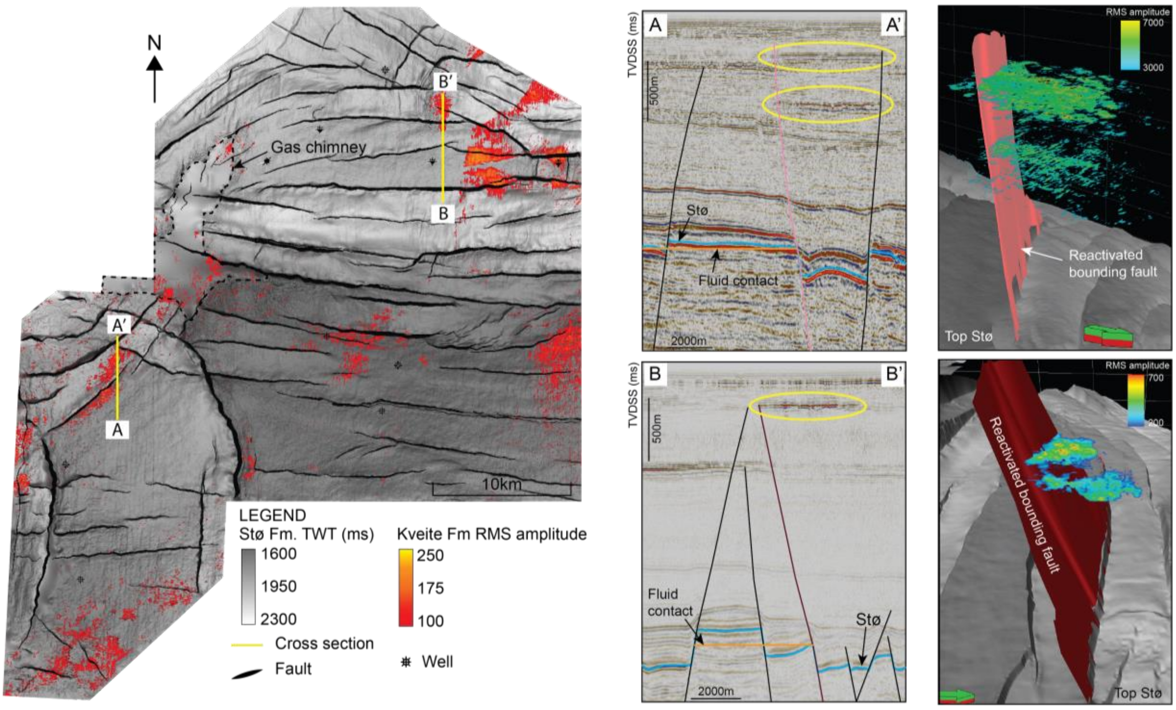

Figure 13